

Unusually Long Duration, Multiple-Doppler Radar Observations of a Front in a Convective Boundary Layer

JOHN R. STONITSCH* AND PAUL M. MARKOWSKI

Department of Meteorology, The Pennsylvania State University, University Park, Pennsylvania

(Manuscript received 17 November 2005, in final form 22 February 2006)

ABSTRACT

Dual-Doppler observations acquired by a network of mobile radars deployed in the Oklahoma panhandle on 3 June 2002 are used to document the kinematic structure and evolution of a front. The data were collected during the International H₂O Project on a mission to study the initiation of deep convection. Synchronized scanning allowed for the synthesis of three-dimensional wind fields for nearly 5.5 h of the 1557–0000 UTC period. The front initially moved southward as a cold front, stalled, and later retreated northward as a warm front. Deep convection failed to be initiated along the front. In situ thermodynamic measurements obtained by a mobile mesonet were used to document changes in the density gradient at the surface. This paper examines the relationships among the changes in baroclinity, the thermally direct frontal circulation, updraft intensity, alongfront updraft variability, and the intensity of vortices along the front.

Increases in the front-normal density gradient tended to be associated with increases in the thermally direct frontal circulation, as expected. Increases in the front-normal density gradient were also associated with an increase in the tilt of the frontal updraft as well as an increase in the contiguity of the updraft along the front, termed the “slabularity.” During periods when the front-normal density gradient and associated thermally direct frontal circulation were weak, the kinematic fields were dominated by boundary layer convection and the slabularity of the front was reduced. Intensification of the front-normal density gradient was accompanied by an increase in the horizontal wind shear and the intensity of vortices that were observed along the front. The vortices modulated the vertical velocity field along the front and therefore the slabularity, too. Thus, although the slabularity was a strong function of the strength of the thermally direct frontal circulation, the slabularity appeared to be modified by vortices in complex ways. Possible implications of the observations for convection initiation are also discussed, particularly with respect to updraft tilt and slabularity.

1. Introduction

One of the principal goals of the International H₂O Project (IHOP; Weckwerth et al. 2004) was to further our understanding of the spatial and temporal variability of water vapor and how this variability affects convection initiation. During an IHOP intensive observing period on 3 June 2002, a wealth of mobile observing systems was deployed in the Oklahoma panhandle in

hopes of observing convection initiation along a front. Convection failed to be initiated along the front, probably because of substantial convective inhibition (CIN). CIN approached 200 J kg⁻¹ on soundings obtained in the vicinity of the front during the late afternoon hours, when CIN is typically at its diurnal minimum.

Although this case may not seem like an enticing convection initiation case—or perhaps even a good convection initiation null case (not even a single cumulus cloud was observed), owing to the rather obvious reason for failure (that being the unfavorable large-scale conditions, which promoted large CIN)—an unusually long duration, dual-Doppler dataset was obtained along the front. High-resolution radar data (125-m grid spacing and 90 s between wind syntheses) collected by four mobile, truck-borne radars afforded over 5 h of dual-Doppler wind syntheses within the

* Current affiliation: American Electric Power, Columbus, Ohio.

Corresponding author address: Dr. Paul Markowski, Dept. of Meteorology, The Pennsylvania State University, 503 Walker Building, University Park, PA 16802.
E-mail: pmarkowski@psu.edu

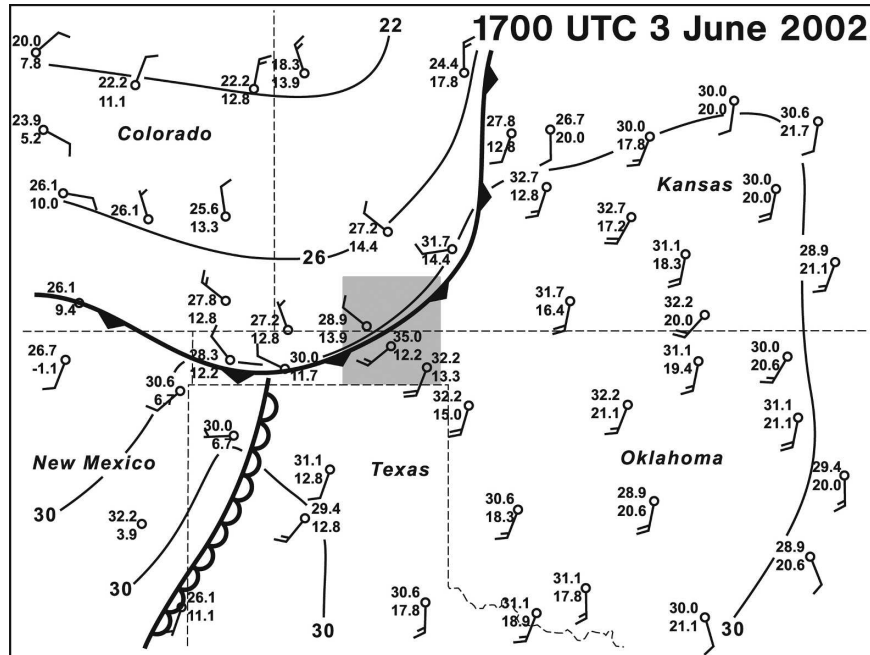


FIG. 1. Surface analysis at 1700 UTC 3 Jun 2002. The thin black lines are isotherms (4°C interval). Temperature ($^{\circ}\text{C}$), dewpoint temperature ($^{\circ}\text{C}$), wind speed (half barb, 2.5 m s^{-1} ; full barb, 5 m s^{-1}), and wind direction are plotted in the station models. The boldface line with filled barbs indicates the cold front and the boldface line with unfilled scallops indicates a dryline. The shaded rectangular region is the region shown in Fig. 5 (left).

1557–0000 UTC period as the front moved slowly southward as a cold front, stalled, and then retreated rapidly northward as a warm front. The purpose of this paper is to document the evolution of the kinematic structure of the front, and how kinematic changes were related to changes in the thermodynamic characteristics of the front. The four-dimensional resolution of the wind field provided by such a network of mobile radars—and the duration of the observations owing to the mobility of the platforms—were not available in many previous studies of the fine structure of fronts. Prior studies have utilized a wide variety of sensors, such as fixed ground-based Doppler radars, serial pibals, rawinsondes, aircraft, and instrumented towers (e.g., Clarke 1961; Martin 1973; Hobbs and Biswas 1979; James and Browning 1979; Carbone 1982; Hobbs and Persson 1982; Parsons and Hobbs 1983; Shapiro 1984; Young and Johnson 1984; Roux et al. 1993; Braun et al. 1997; Yu and Smull 2000; Wakimoto and Bosart 2000, 2001).

The paper is organized as follows. Section 2 contains an overview of the 3 June 2002 IHOP case. Section 3 describes the data and analysis techniques. Section 4 describes the dual-Doppler observations. Section 5 discusses aspects of this case that might be pertinent to the initiation of deep convection. Finally, section 6 presents

a summary, conclusions, and possible avenues for future research.

2. Overview of the 3 June 2002 IHOP case

The IHOP mobile observing facilities were deployed during the midmorning hours to the Oklahoma panhandle, where a weak cold front was observed to be moving slowly southeastward (Fig. 1).¹ The slowly moving front was deemed to be the most likely location for convection initiation, although the expectations for initiation were low, given relatively warm air aloft (e.g., 700-mb temperatures of $13^{\circ}\text{--}15^{\circ}\text{C}$ were observed in the vicinity of the front) and only modest boundary layer moisture (specific humidities were generally less than 10 g kg^{-1}), which combined to yield large CIN. Throughout the late morning and afternoon hours, no boundary layer cumulus clouds were observed to develop, probably as a result of the large CIN. Cirrus clouds increased in areal coverage and thickened within the data collection region after approximately 1800 UTC, significantly limiting insolation and further limiting the prospects for the initiation of convection along

¹ All times are given in UTC, which was 6 h ahead of local standard time.

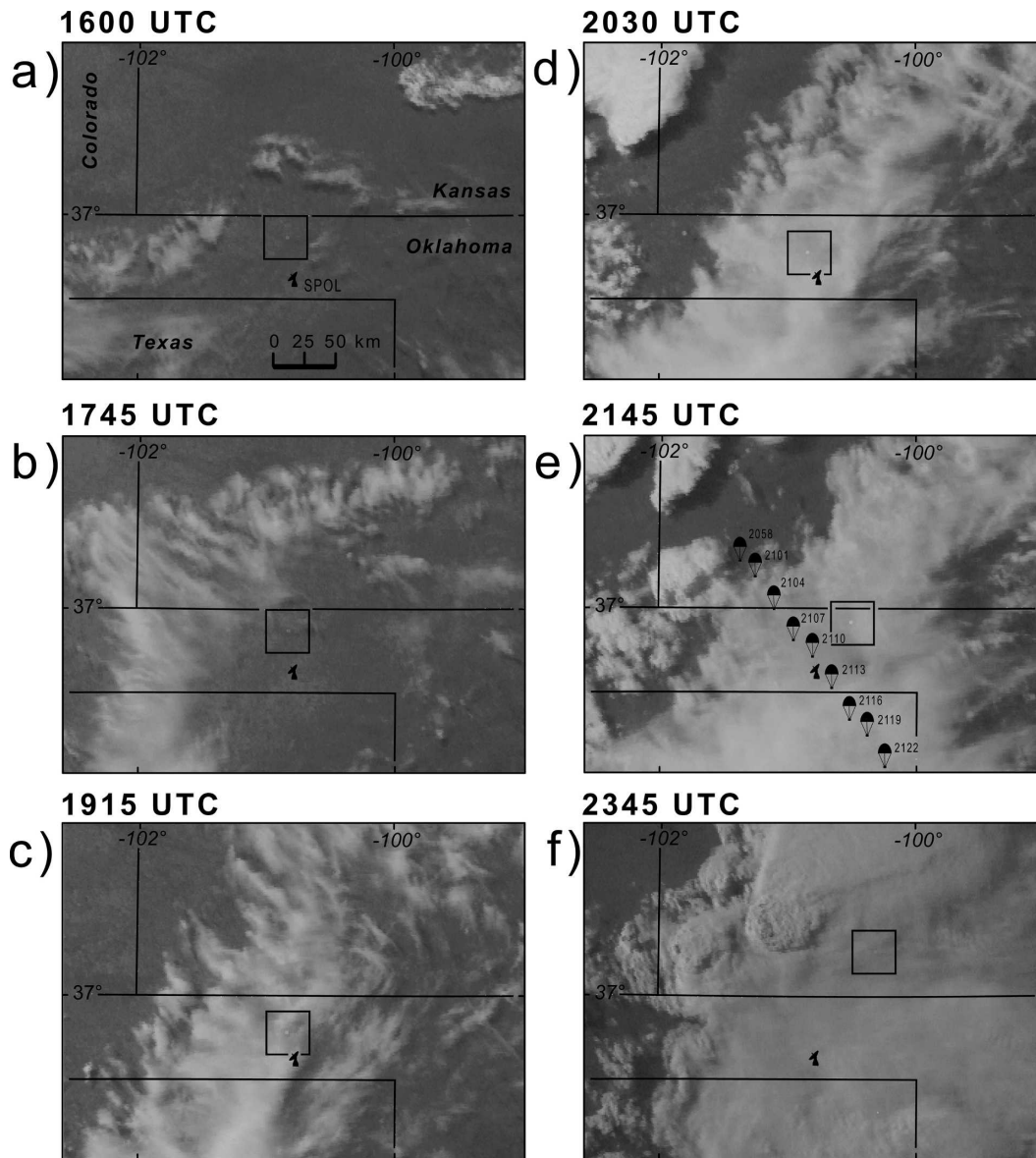


FIG. 2. Visible satellite imagery at (a) 1600, (b) 1745, (c) 1915, (d) 2030, (e) 2145, and (f) 2345 UTC. The location of the dual-Doppler wind synthesis domain at the time of each satellite image is outlined with a square. The location of the SPOL radar is also indicated. The locations and times (UTC) of the dropsondes used in Figs. 3 and 6 are indicated in (e).

the front (Fig. 2). Even by late afternoon, when CIN is typically near its diurnal minimum, dropsondes² indicated that considerable CIN ($>170 \text{ J kg}^{-1}$) had to be overcome in order for the level of free convection (LFC) to be attained by parcels originating in the boundary layer (Fig. 3).

The front was easily visible as a fine line in radar

² The dropsondes were released by the Flight International Learjet, which operated on most IHOP missions (Hock and Franklin 1999).

reflectivity data from the National Center for Atmospheric Research (NCAR) S-band dual-polarization Doppler radar (SPOL; Fig. 4) that was located in the eastern Oklahoma panhandle, generally less than 50 km from where the mobile radars were operating. From the start of data collection by the mobile radars (1557 UTC) until approximately 2045 UTC, the front moved southeastward as a cold front (Figs. 4 and 5). From 2045 to 2115 UTC, the front was approximately stationary. A cross section approximately normal to the front was constructed from dropsondes released between 2058

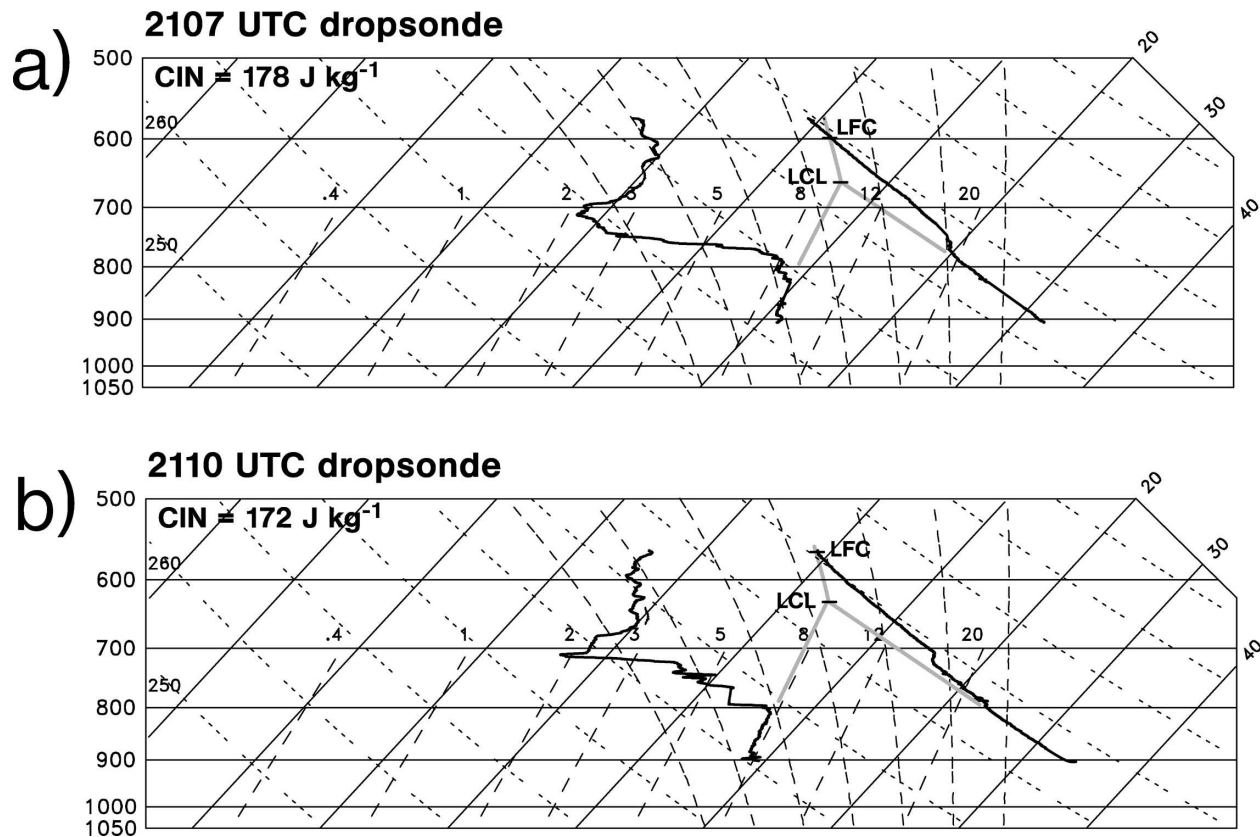


FIG. 3. Skew T - $\log p$ diagrams of the soundings obtained from the dropsondes launched at 2107 and 2110 UTC. Isobars (solid) are drawn at 100-mb intervals, isotherms (solid) are drawn at 10°C intervals, isentropes (solid) are drawn at 20-K intervals, pseudoadiabats (dashed) are drawn at 8°C intervals, lines of constant water vapor mixing ratio line (dashed) are also included (0.4, 1, 2, 3, 5, 8, 12, and 20 g kg^{-1}). The heights of the LCL and LFC also are indicated, as is the amount of CIN, for a lifted parcel having the mean thermodynamic properties of the lowest 100 mb. The locations of the dropsondes are indicated in Figs. 2 and 4.

and 2122 UTC. The cross section revealed the presence of a narrow corridor of dry boundary layer air immediately south of the front (Fig. 6), consistent with moisture fields derived indirectly from SPOL refractivity measurements (Stonitsch and Markowski 2004). The boundary layer was also noticeably deeper on the warm side of the front than on its cool side.

Thunderstorms developed well north of the front on the high plains of western Kansas and eastern Colorado after 2000 UTC (Fig. 2d), but failed to form along the front within the region observed with the mobile radars. The initiation of these storms was likely heavily influenced by topographic effects. Thunderstorms are commonly initiated on the relatively high terrain of western Kansas and eastern Colorado in the absence of obvious mesoscale convergence lines, especially on the cool side of synoptic-scale fronts, where the air mass is frequently moister than the air mass south of the fronts, as was the case on 3 June 2002 (Fig. 1).

After 2115 UTC, the front retreated northwestward as a warm front, probably in response to pressure falls

associated with the amplification of a Rocky Mountain lee trough to the west. The front accelerated in time (Figs. 4 and 5), such that by the end of the data collection period (approximately 0000 UTC), the front was moving northwestward at approximately 12 m s^{-1} . The prominence of the reflectivity fine line had diminished significantly by 0000 UTC as well (Fig. 4f), although much of the fading of the fine line was a result of the increasing range from the SPOL radar (the fine line was still apparent in the mobile radar data, although the fine line was not as evident as at earlier times).

The 3 June 2002 IHOP intensive observing period consisted of four mobile radar deployments (Fig. 5) from 1557 to 0000 UTC. The deployment locations were dictated by the motion of the front and by logistical considerations, such as the road network and terrain. Over 5 h of dual-Doppler radar observations were obtained as the front meandered southeastward and northwestward during the approximately 8-h mission (Table 1). A description of the nature of the radar observations, as well as the analysis techniques employed

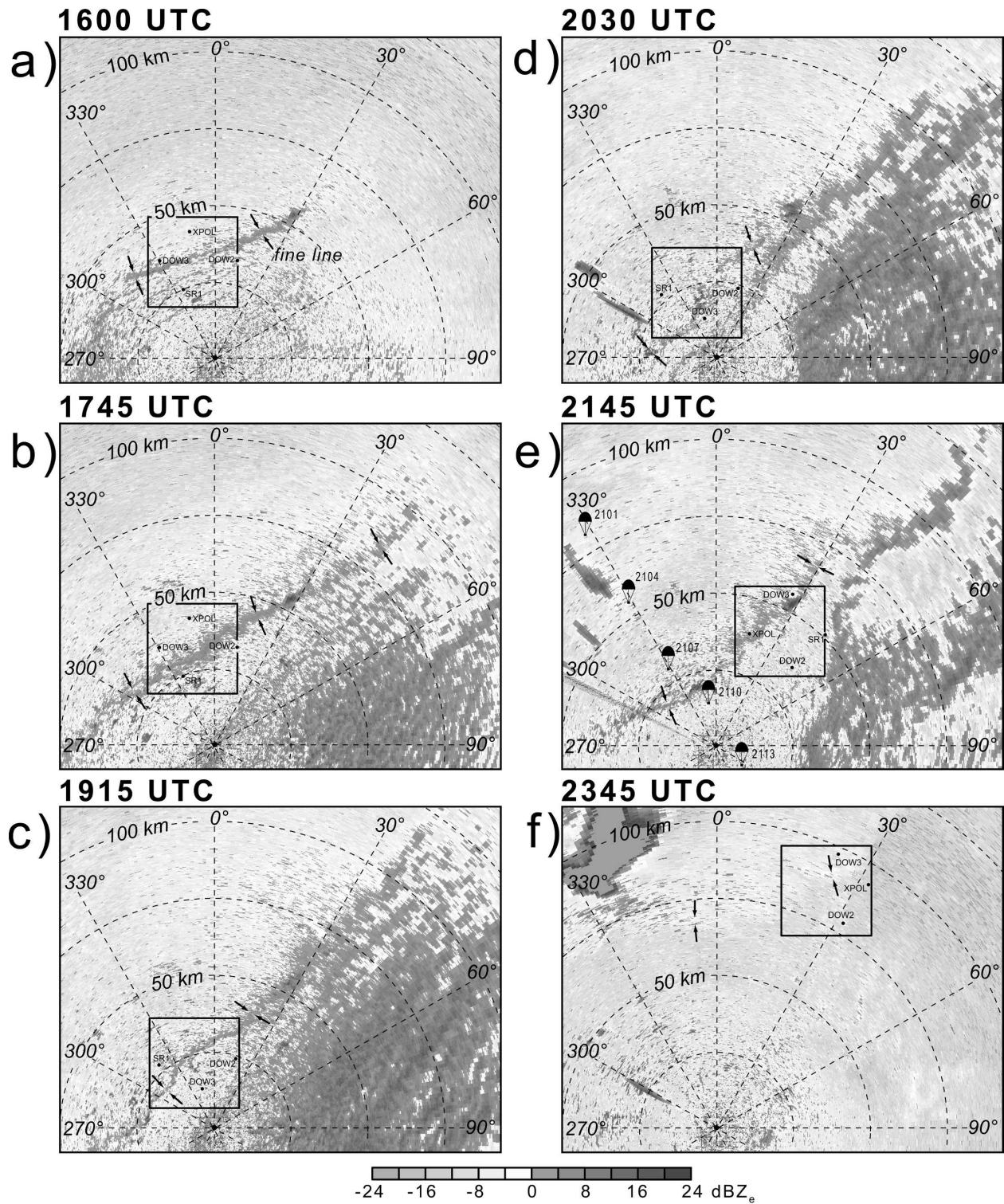


FIG. 4. Equivalent radar reflectivity factor from the SPOL radar at (a) 1600, (b) 1745, (c) 1915, (d) 2030, (e) 2145, and (f) 2345 UTC. The reflectivity fine line associated with the front is indicated, as are the locations of the mobile Doppler radars and dual-Doppler wind synthesis domains. The locations and times (UTC) of the dropsondes used in Figs. 3 and 6 are indicated in (e).

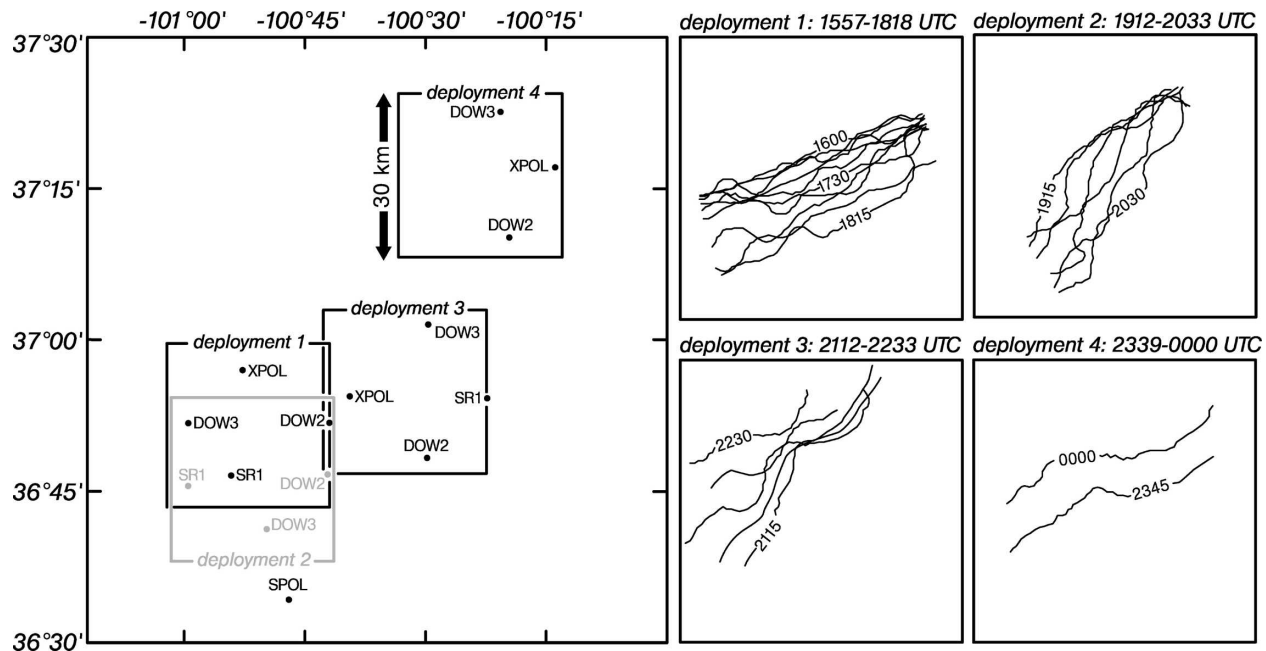


FIG. 5. (large left panel) Dual-Doppler wind synthesis domains for deployments 1–4 (also see Figs. 2 and 4). The positions of the radars also are indicated. The domain and radar positions for deployment 2 are in gray so that they may be distinguished from those of deployment 1. (four smaller right panels) Isochrones of the frontal boundary at 15-min intervals in each of the four deployments.

to construct three-dimensional wind fields, is provided in the next section.

3. Data and analysis methods

a. Mobile radar data and three-dimensional wind synthesis

Four mobile radars collected data during four separate deployments within the 1557–0000 UTC period

(Table 1; Fig. 5). Three of the mobile radars [two Doppler On Wheels (DOW2 and DOW3) radars and the University of Connecticut X-band dual-polarimetric radar (XPOL)] were similar to those described by Wurman et al. (1997). The wavelength, stationary half-power beamwidth, and Nyquist velocity were 3 cm, 0.93°, and 16.0 m s⁻¹, respectively. Volumes were completed every 90 s, during which time 16 elevation angles were scanned from 0.5° to 14.5°. The azimuth interval

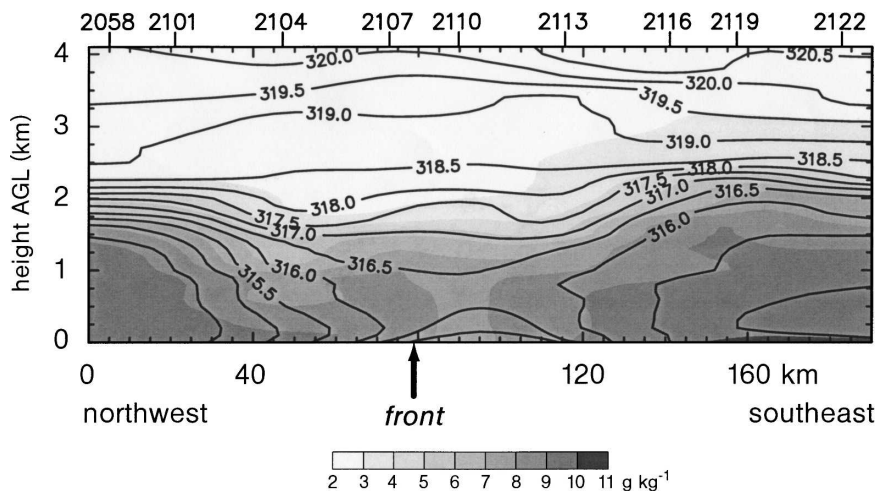


FIG. 6. Cross section of virtual potential temperature (solid contours; 0.5-K interval) and water vapor mixing ratio (shaded; see legend). The locations of each of the dropsondes used to construct the cross section are indicated along the top of the cross section and in Figs. 2 and 4.

TABLE 1. Summary of the mobile radar deployments having dual-Doppler coverage. A range is given for the number of radars contributing to the dual-Doppler wind syntheses because the exact number varied throughout each deployment. When >2 radars were available at an analysis time, the three-dimensional wind field was synthesized using overdetermined dual-Doppler techniques.

Deployment No.	Time (UTC)	Duration (min)	No. of radars
1	1557–1818	141	2–4
2	1910–2033	83	2–3
3	2112–2233	81	2–4
4	2339–0000	21	2–3

between each ray was 0.7° . The average data spacing within the analysis region was approximately 150 m in the horizontal and 175 m in the vertical (note the oversampling implied by the sampling intervals in azimuth and elevation angle). The fourth mobile radar [the Shared Mobile Atmospheric Research and Teaching (SMART) radar (SR1)] has been described by Biggerstaff et al. (2005). The wavelength, stationary half-power beamwidth, and Nyquist velocity were 5 cm, 1.5° , and 14.6 m s^{-1} , respectively. Volumes were completed every 180 s, during which time 15 elevation angles were scanned from 0.5° to 25.2° . The azimuth interval between each ray was 1.0° . Within the analysis region, the average data spacing was approximately 200 m in the horizontal and 250 m in the vertical.

Mobile radar data first were rotated to the correct azimuth using a combination of solar alignment (Arnott et al. 2003), when available, and georeferencing using identifiable ground clutter targets such as relay towers and power lines. Such rotations were necessary because data were collected in truck-relative coordinates. Once rotated, spurious data caused by low signal-to-noise ratio, velocity aliasing, second-trip echoes, and ground clutter were removed. The NCAR Reorder software was used to interpolate edited radar data from each deployment onto a $30 \text{ km} \times 30 \text{ km} \times 1.5 \text{ km}$ Cartesian grid having a horizontal and vertical grid spacing of 125 m. The lowest grid level was placed at the mean elevation of the radars.

The interpolation of the radial velocity data to the grids was accomplished by way of a Barnes objective analysis (Barnes 1964; Koch et al. 1983), using an isotropic, spherical weight function and smoothing parameter κ of 0.25 km^2 . The choice of κ was based on the coarsest data sampling within the wind synthesis domain, following the conservative recommendations of Trapp and Doswell (2000), whereby $\kappa = (1.33 \times \Delta d)^2$ was used (Pauley and Wu 1990), where Δd was the coarsest data spacing within an analysis region. Radial

wind velocity structures having wavelengths less than 4 times the data spacing were severely damped by the objective analysis procedure. For computational reasons, data beyond a “cutoff” radius of 1.25 km from each grid point were not considered in the calculation of the weights, even though the theoretical contribution to the weight function remains nonzero and positive, albeit very small, for distances between a datum and grid point approaching infinity. The sensitivity of the wind syntheses to κ is investigated in the appendix. Finally, movement of features during the collection of a radar data volume was removed from the objectively analyzed radial velocity grids using Matejka’s (2002) technique for determining the reference frame velocity. This correction prevents features from acquiring an artificial downwind tilt with height due to translation that occurs during the time it takes to complete a volume scan.

Three-dimensional wind syntheses were produced by NCAR’s Custom Editing and Display of Reduced Information in Cartesian Space (CEDRIC; Mohr et al. 1986) software using standard dual-Doppler techniques. When more than two radars were available at an analysis time, the overdetermined dual-Doppler approach and the anelastic mass continuity equation (integrated upward) were used, rather than a direct triple- or quadruple-Doppler solution. The former approach has several advantages over the latter approaches, as demonstrated by Kessinger et al. (1987), especially when elevation angles are confined to the lowest approximately 15° – 25° . Comparisons between the synthesized wind fields and in situ wind measurements (e.g., observations from the research aircraft participating in IHOP), where available (and smoothed so that the scales represented in the velocity time series were comparable to those resolved in the radar-derived wind syntheses), indicated good agreement between the radar-derived wind fields and those measured directly.

The time resolution of the wind syntheses is 90 s, and 218 wind syntheses cover nearly 70% of the 1557–0000 UTC period (data collection must be forfeited while radars are being redeployed in order to keep pace with the motion of the front). We believe that such long-duration, high-temporal-resolution dual-Doppler observations of a single phenomenon (5 h and 26 min of three-dimensional wind syntheses at 90-s intervals) may be unprecedented.

b. Objectively defining the position of the front

For many of the analyses conducted herein, it was necessary to have a means by which the position of the front could be objectively defined. The front was objectively defined by the path that traced the relative

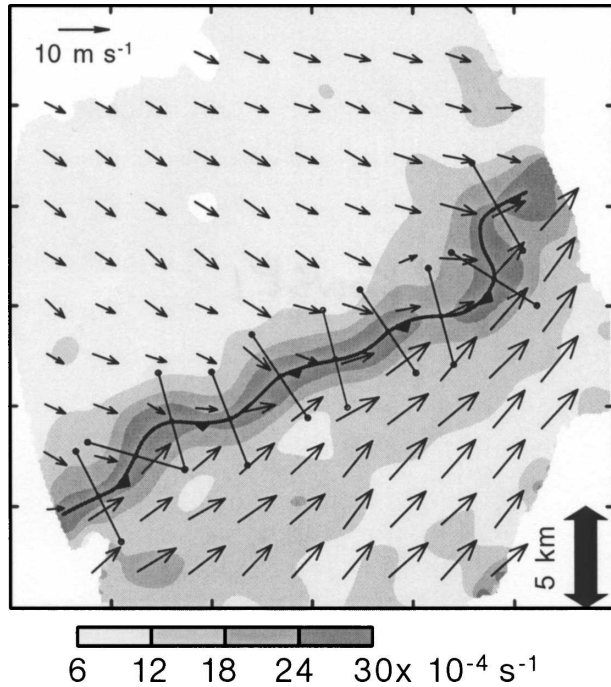


FIG. 7. Horizontal cross section of the magnitude of the horizontal velocity gradient tensor (shaded) at the lowest grid level at 1800 UTC. The relative maximum in the field is used to objectively define the position of the front, which has been drawn using conventional symbols (i.e., bars). The 5-km-long line segments that bisect the front indicate the segments over which the mean front-normal temperature gradient was computed. Horizontal wind vectors at the lowest grid level also are drawn (the tail of each vector is located at every 20th grid point), and their length is scaled by the wind speed.

maximum in the magnitude of the horizontal velocity gradient tensor ($|\nabla_h \mathbf{v}_h|$, where \mathbf{v}_h is the horizontal velocity vector) at the lowest grid level, where, using Einstein summation notation,

$$|\nabla_h \mathbf{v}_h| = \sqrt{\frac{1}{2} \sum_{i=1}^2 \sum_{j=1}^2 \left(\frac{\partial u_i}{\partial x_j} \right)^2}. \quad (1)$$

The $|\nabla_h \mathbf{v}_h|$ field at 1800 UTC is shown as an example (Fig. 7). Notice that the objectively defined frontal position nicely follows kinks and bends in the wind shift line. Although it might be preferable to define the position of a front based on the density gradient or changes in the density gradient (Sanders and Doswell 1995), the vast superiority of the coverage and resolution of radar-derived kinematic observations compared with thermodynamic observations argued for a wind shift-based criterion.

c. Mobile mesonet observations

Nine automobile-borne surface observing systems, which composed a “mobile mesonet” (Straka et al.

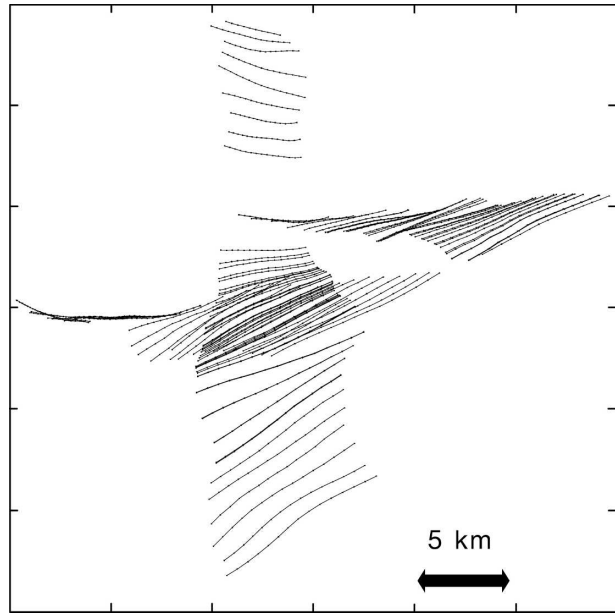


FIG. 8. Trajectories passing through the locations of mobile mesonet observations during the 1557–1612 UTC period.

1996), obtained temperature, relative humidity pressure, and wind velocity measurements within the wind synthesis domains. These in situ observations were used to assess the evolution of density gradients in the vicinity of the front. To reduce the data voids that unavoidably arise (the automobiles can only obtain data along roads), trajectories were computed 7.5 min forward and backward in time from the locations of mobile mesonet observations. The trajectories were computed using the radar-derived wind syntheses at the lowest grid level (Fig. 8). Virtual potential temperature θ_v was assumed to be conserved along the trajectories. Thus, the trajectories extended the mobile mesonet observations of θ_v into regions where no observations were obtained directly. The θ_v values were then objectively analyzed using $\kappa = 1 \text{ km}^2$. This approach follows that which has been described by Buban et al. (2003). It is worth noting that this method of extending data into data-sparse regions is probably what a good subjective analyst tasked with drawing θ_v contours from raw data alone would do anyway, perhaps without even realizing it. The approach naturally tends to result in θ_v contours that are approximately parallel to the front, as might be expected. In other words, the approach retains one of the primary advantages of objective analysis—reproducibility—yet also incorporates information about airmass boundaries via tracing conserved quantities along trajectories, which a traditional objective analysis does not do.

The magnitude of the mean front-normal gradient of

virtual potential temperature, $|\overline{\partial\theta_v/\partial n}|$ (n increases toward the colder air), which is a measure of the baroclinity of the front, was computed using the objectively analyzed θ_v fields from the mobile mesonet and the objectively defined front position. An estimate of $|\overline{\partial\theta_v/\partial n}|$ was obtained at each analysis time by averaging finite differences of θ_v taken at approximately a dozen equally spaced locations along the front. The differences were computed over line segments centered on the front and oriented orthogonally to the front (Fig. 7). Dynamic retrievals of buoyancy also were attempted using the three-dimensional wind syntheses (e.g., Gal-Chen 1978; Hane and Ray 1985), but the results were often suspect when compared with direct observations. It is possible that the poor agreement owed to rapid temporal evolution of the wind fields within the convective boundary layer (such retrievals are sensitive to the resolution of velocity time derivatives).

d. Circulation calculations

Circulation was computed around closed curves straddling the front, lying within both horizontal and vertical planes. The circulation about a vertical axis Γ_v was computed along an approximately $10 \text{ km} \times 25 \text{ km}$ circuit located at the lowest grid level, straddling the front in a horizontal plane (the alongfront dimension of the circuit is only approximately 25 km owing to the fact that the circuit was forced to conform to the bends in the frontal boundary; the area of the circuit was constrained to be a constant at all analysis times). Via Stokes's theorem,

$$\Gamma_v = \int_S \zeta dA, \tag{2}$$

where S is the two-dimensional surface bounded by the circuit along which circulation was computed, ζ is the vertical component of the vorticity, and dA is the area element on S . It is clear from (2) and the specification of S that Γ_v is proportional to the mean vertical vorticity at the lowest grid level within 5 km of the front.

Similarly, the circulation about a horizontal axis Γ_h was computed by averaging the circulation about three separate $1 \text{ km} \times 10 \text{ km}$ circuits lying in vertical planes, bisected by the front (Γ_h was computed at three locations and averaged in order to minimize its sensitivity to the choice of an unrepresentative cross section). The circulation about each of the three circuits is

$$\Gamma_h = \int_S \boldsymbol{\omega}_h \cdot \mathbf{n} dA, \tag{3}$$

where the $\boldsymbol{\omega}_h$ is the horizontal vorticity vector and \mathbf{n} is the unit vector normal to S . From (3) and the specifi-

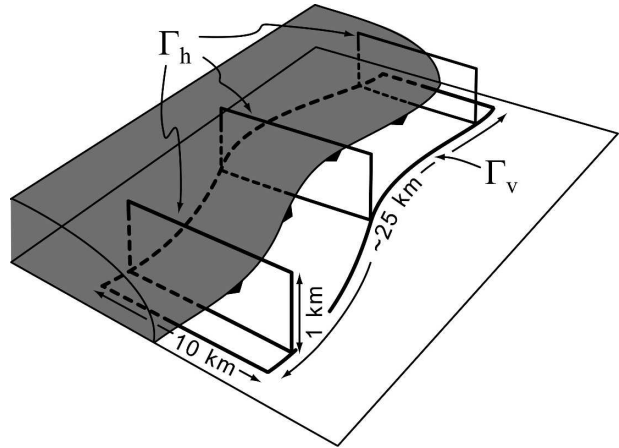


FIG. 9. Schematic illustrating the circuits along which the vertical and horizontal circulation was computed. The vertical circulation Γ_v was computed along an approximately $10 \text{ km} \times 25 \text{ km}$ circuit located at the lowest grid level, straddling the front in a horizontal plane (the alongfront dimension of the circuit is only approximately 25 km owing to the fact that the circuit was forced to conform to the bends in the frontal boundary; the length of the circuit was constrained to be a constant at all analysis times). The horizontal circulation, Γ_h , was computed by averaging the circulation about three separate $1 \text{ km} \times 10 \text{ km}$ circuits bisecting the front in vertical planes.

cation of S , it is apparent that Γ_h is proportional to the mean, front-parallel, horizontal vorticity within the lowest 1 km and within a 5-km horizontal distance of the front. An illustration of the curves about which Γ_v and Γ_h were computed is shown in Fig. 9.

4. Dual-Doppler observations of the front

a. Summary of observations

One of the most obvious observations throughout the four deployments was the complexity of the kinematic structure of the front. This may not be surprising, given the resolution of the four-dimensional wind field afforded by the mobile radar network used herein. The front continually displayed kinks and wavelike structures, examples of which can be seen in the isochrone analyses and in the vertical velocity and vorticity fields (Figs. 5 and 10). It is well known that interactions between fronts and rugged terrain can spawn some of the complex structures observed; however, these observations were made in a region of very little (<50 m) topographic relief. We cannot address what dynamics were responsible for the complex frontal structure, although, at times, the radar reflectivity fine line had an appearance similar to the leading edge of a density current that succumbs to lobe and cleft instability (Simpson 1969).

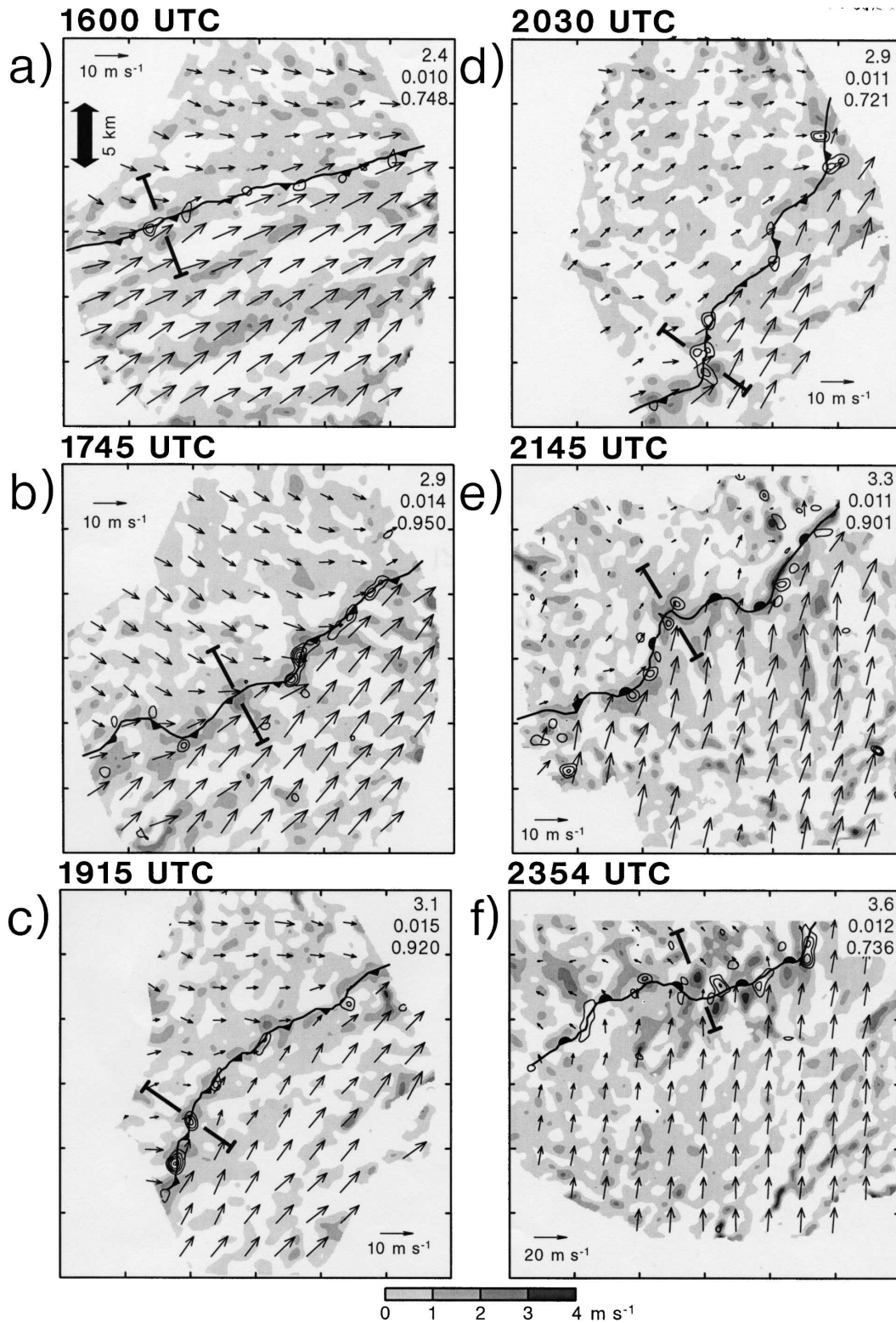


FIG. 10. Horizontal cross sections showing regions of updraft at 750 m (shaded) and vorticity maxima at the lowest grid level (solid contours are drawn every $2.5 \times 10^{-3} \text{ s}^{-1}$, starting at $5.0 \times 10^{-3} \text{ s}^{-1}$) at (a) 1600, (b) 1745, (c) 1915, (d) 2030, (e) 2145, and (f) 2354 UTC. Horizontal wind vectors at the lowest grid level also appear (the tail of each vector is located at every 20th grid point), and their length is scaled by the wind speed. The objectively determined positions of the front have been overlaid using conventional symbols. The three numbers at the top-right corner indicate the maximum vertical velocity (m s^{-1}) at 750 m along the front, the maximum vertical vorticity (s^{-1}) at the lowest grid level along the front, and the slabularity, respectively. The locations of the cross sections appearing in Fig. 18 also are indicated. The locations of the dual-Doppler wind synthesis domains can be viewed in Figs. 2, 4, and 5.

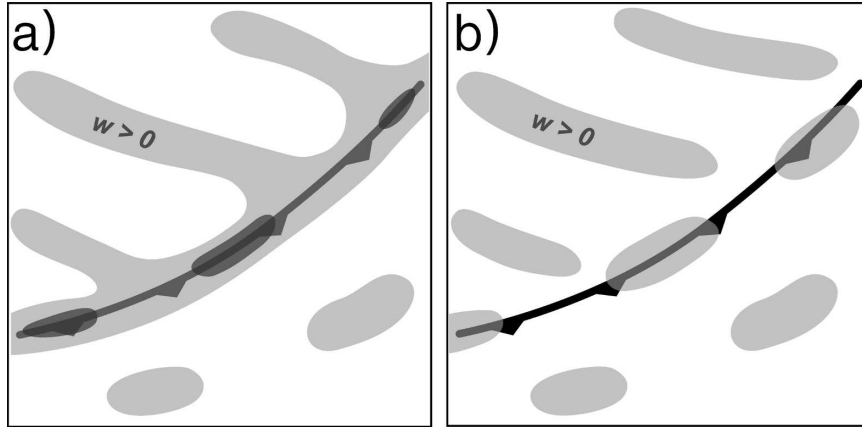


FIG. 11. Schematic illustrating regions of updraft (shaded; dark shading indicates strongest updrafts) when (a) the thermally direct frontal circulation is a large contributor to the total vertical motion field (large slabularity) and when (b) the thermally direct frontal circulation is a small contributor to the total vertical motion field (small slabularity), compared with the motions associated with boundary layer convection.

The contribution of boundary layer convective cells to the kinematic fields is also clearly evident (e.g., Fig. 10). Although the maximum vertical velocities generally were observed along the front, the vertical velocity fields also reveal structures away from the front that were associated with boundary layer thermals. The vertical velocities in the strongest cells were 3–4 m s⁻¹ at 750 m, which equaled the peak vertical velocities observed along the front at the same altitude (Fig. 10). During several periods (e.g., Figs. 10a,d), because of the prominence of boundary layer convective motions relative to the motions driven by frontal dynamics, one would likely find it challenging to identify the front by inspection of the vertical velocity field alone.

The influence of boundary layer convection on the vertical velocity field, relative to the influence of the thermally direct frontal circulation, affects the degree of updraft contiguity along the front. Notice in Fig. 10 that the front is associated with a nearly unbroken corridor of updraft at some times (e.g., Fig. 10b), and at other times, significant alongfront vertical velocity variability exists such that an unbroken corridor of updraft is not observed (e.g., Fig. 10a). A parameter termed “slabularity” was computed as a means of quantifying the contiguity of the updraft along the front.³ The slabularity S is the fraction of points along the objectively defined front at which an updraft is observed, that is,

$$S = \frac{1}{N_f} \sum_i H(w_i), \quad (4)$$

³ James et al. (2005) have used the adjective slabular to describe nearly unbroken lines of updraft along thunderstorm gust fronts.

where N_f is the number of points that define the objectively defined front (approximately five points per kilometer), w_i is the vertical velocity at the i th point along the front (at 750 m AGL, although S was found to be insensitive to the altitude from which w_i was obtained), and $H(w_i)$ is the Heaviside step function

$$H(w_i) = \begin{cases} 0, & w_i \leq 0 \\ 1, & w_i > 0 \end{cases} \quad (5)$$

A (maximum) slabularity of unity implies that an updraft spans the entire length of the front, which might be expected to be the case when frontal dynamics are very dominant (Fig. 11a). A slabularity of 0.5 implies that only half of the length of the front is occupied by updraft, which might be anticipated when convective motions have a relatively large influence on the kinematic fields (Fig. 11b).

In the remaining subsections, observations that are specific to each of the four deployments are presented.

b. Deployment 1: 1557–1818 UTC

The front moved slowly southward at 1–2 m s⁻¹ during the early portion of the deployment. Its southward motion accelerated to ~3 m s⁻¹ by the end of the deployment (Fig. 5). Wind directions south of the front near the surface were approximately 230°–250°, shifting to 260°–310° north of the front (Figs. 10a,b). The wind shift increased in time as the first deployment progressed, as did $|\partial\theta_v/\partial n|$, which approximately doubled from 1.8 K (10 km)⁻¹ to 3.7 K (10 km)⁻¹ between 1557 and 1745 UTC (Figs. 12a,b and 13).

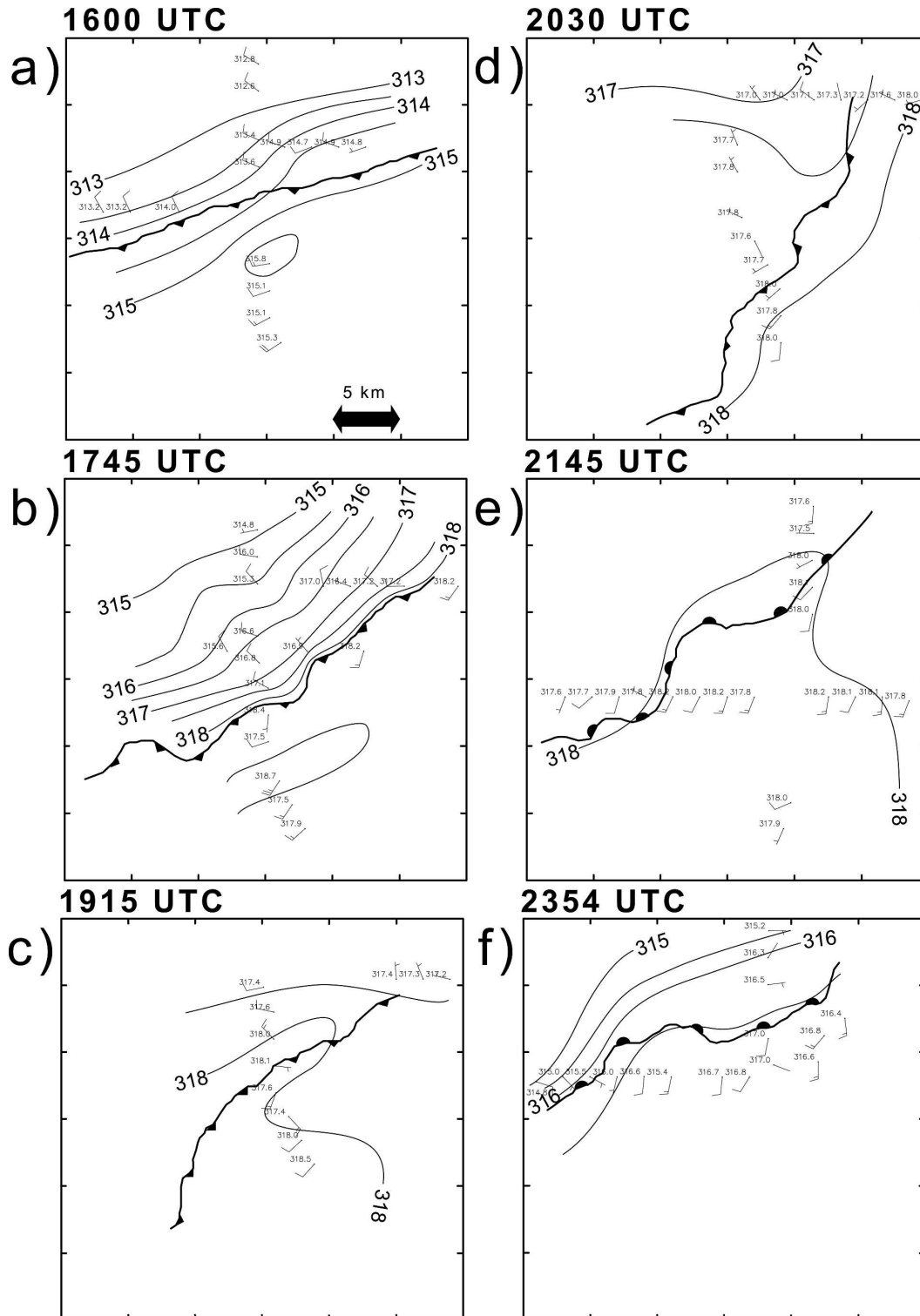


FIG. 12. Surface observations made by the mobile mesonet within the dual-Doppler wind synthesis domain at (a) 1600, (b) 1745, (c) 1915, (d) 2030, (e) 2145, and (f) 2354 UTC. Observations obtained within 5 min of each analysis time are included. The objectively determined positions of the front have been overlaid as in Fig. 10. Virtual potential temperature (K) and wind speed (half barb, 2.5 m s^{-1} ; full barb, 5 m s^{-1}) and direction are plotted in the station models. Virtual potential temperature is contoured at 0.5-K intervals, based on the enhanced objective analysis procedure described in the text. The locations of the dual-Doppler wind synthesis domains can be viewed in Figs. 2 and 5.

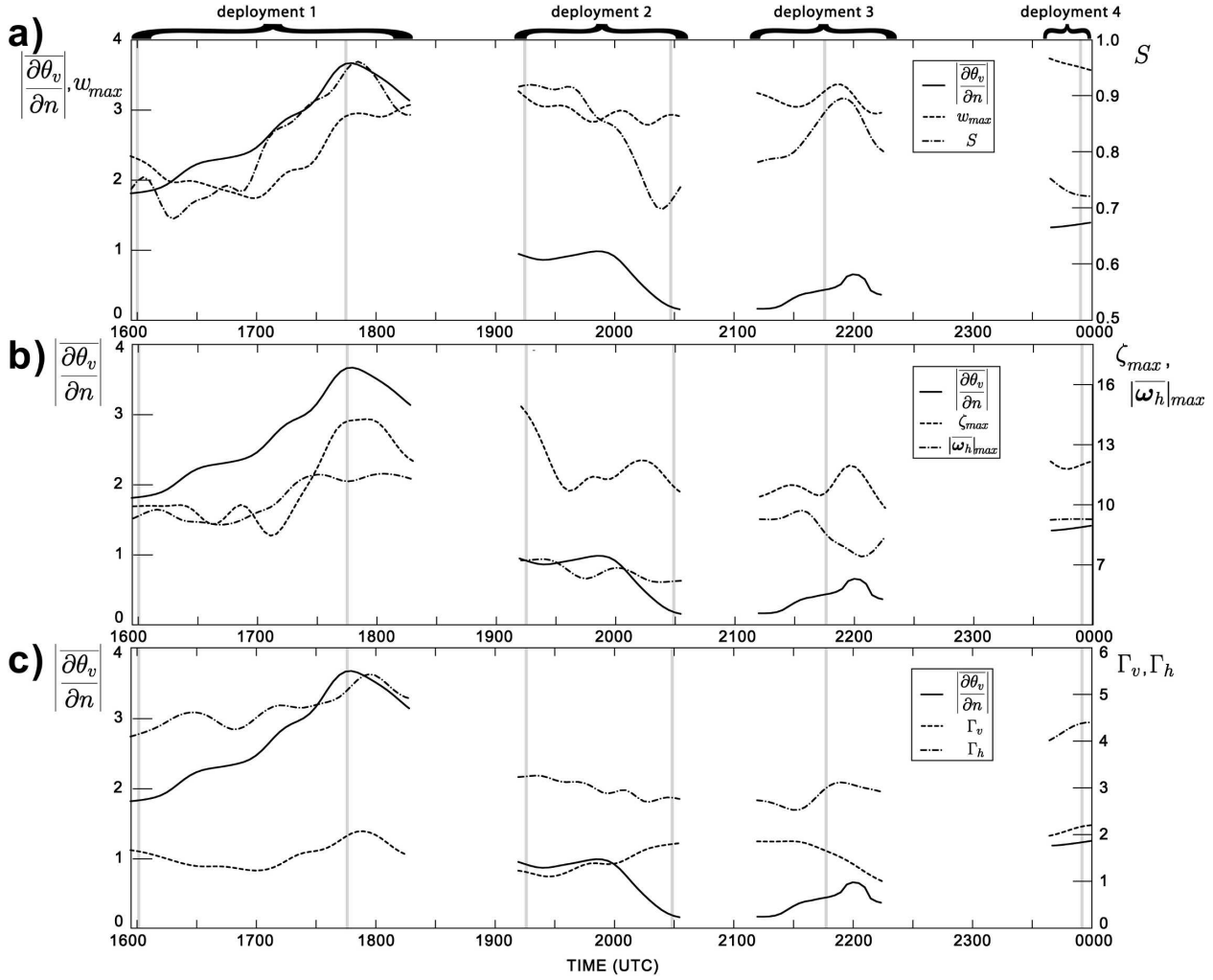


FIG. 13. (a) Time series of $|\overline{\partial\theta_v/\partial n}|$ [$\text{K} (10 \text{ km})^{-1}$; scale is on the left ordinate], S (scale is on the right ordinate), and w_{\max} (m s^{-1} ; scale is on the left ordinate) along the front. The gray vertical lines indicate the times of the analyses presented in Figs. 10, 12, 14, and 15. (b) Time series of $|\overline{\partial\theta_v/\partial n}|$ [$\text{K} (10 \text{ km})^{-1}$; scale is on the left ordinate], ζ_{\max} ($\times 10^{-3} \text{ s}^{-1}$; scale is on the right ordinate), and $|\overline{\omega_h}|_{\max}$ ($\times 10^{-3} \text{ s}^{-1}$; scale is on the right ordinate). The gray vertical lines have the same meaning as in (a). (c) Time series of $|\overline{\partial\theta_v/\partial n}|$ [$\text{K} (10 \text{ km})^{-1}$; scale is on the left ordinate], Γ_v ($\times 10^5 \text{ m}^2 \text{ s}^{-1}$; scale is on the right ordinate), and Γ_h ($\times 10^5 \text{ m}^2 \text{ s}^{-1}$; scale is on the right ordinate). Refer to Fig. 9 for a more detailed explanation of Γ_v and Γ_h . The gray vertical lines have the same meaning as in (a).

The increase in $|\overline{\partial\theta_v/\partial n}|$ was likely a result of the horizontal deformation, which also increased in time throughout deployment 1, acting frontogenetically on the existing θ_v field (Fig. 14). Contours of the scalar frontogenesis F_n , computed using the mobile mesonet-derived θ_v field and dual-Doppler wind syntheses at the lowest grid level, are included in Fig. 14:

$$F_n = -\frac{1}{|\nabla_h \theta_v|} \left[\frac{\partial \theta_v}{\partial x} \left(\frac{\partial u}{\partial x} \frac{\partial \theta_v}{\partial x} + \frac{\partial v}{\partial x} \frac{\partial \theta_v}{\partial y} \right) + \frac{\partial \theta_v}{\partial y} \left(\frac{\partial u}{\partial y} \frac{\partial \theta_v}{\partial x} + \frac{\partial v}{\partial y} \frac{\partial \theta_v}{\partial y} \right) \right], \quad (6)$$

where $\nabla_h \theta_v$ is the horizontal gradient of virtual potential temperature, u and v are the zonal and meridional wind components, and

$$\mathbf{F} = \frac{d\nabla_h \theta_v}{dt} = F_n \mathbf{n} + F_s \mathbf{s}, \quad (7)$$

where \mathbf{F} is the frontogenesis vector, F_n represents the frontogenetical component of \mathbf{F} , F_s is the rate of change of the direction of \mathbf{F} due to rotation, and \mathbf{n} and \mathbf{s} are unit vectors in the front-normal and alongfront directions, respectively (\mathbf{n} points toward the cold air and \mathbf{s} points 90° to the right of \mathbf{n} ; Keyser et al. 1988). Differ-

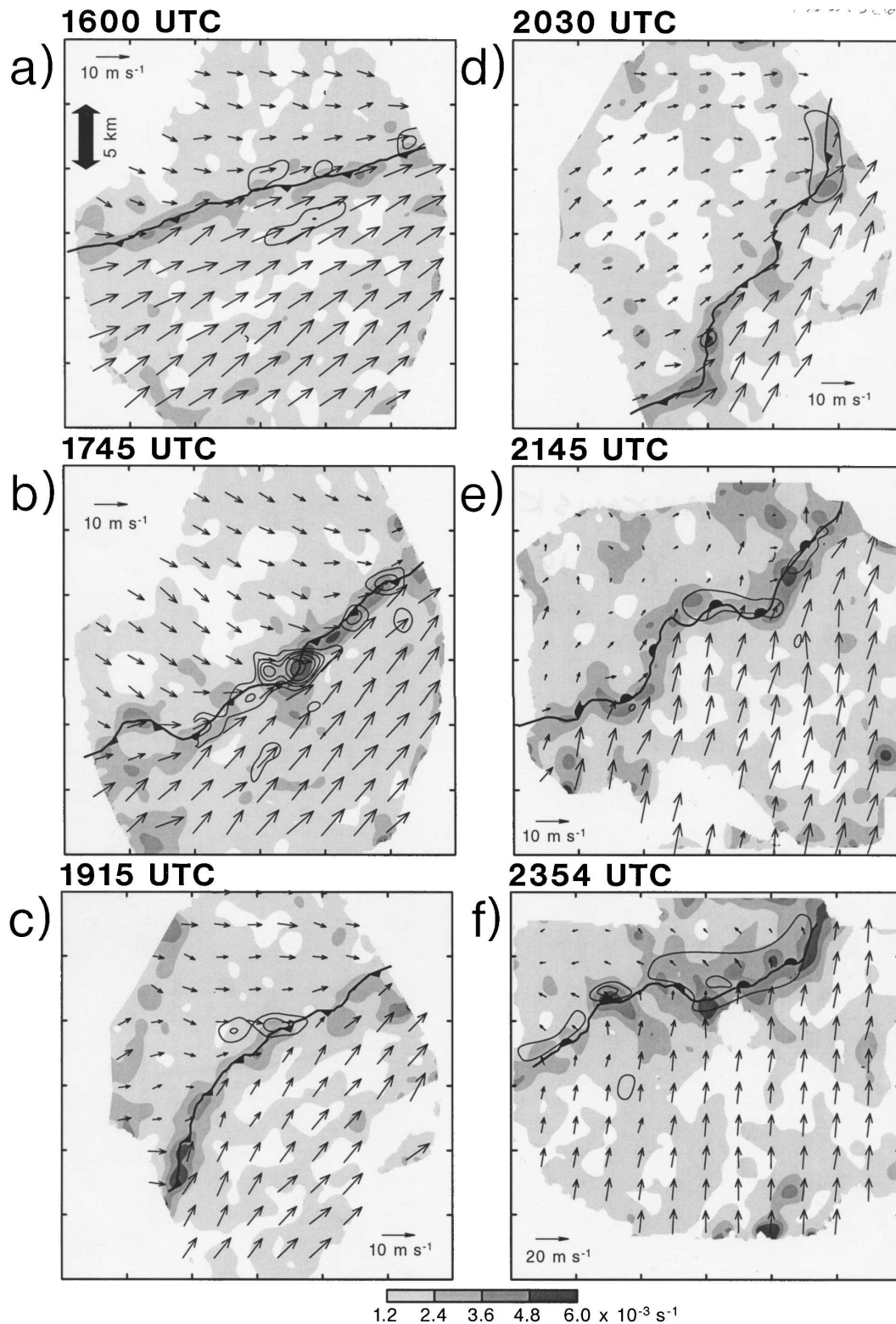


FIG. 14. Horizontal cross sections of the magnitude of the deformation in the horizontal plane at the lowest grid level (shaded) and scalar frontogenesis computed from the radar-synthesized wind field at the lowest grid level and mobile mesonet analyses of virtual potential temperature displayed in Fig. 12 (solid contours are drawn every 1 K km⁻¹ h⁻¹, starting at 1 K km⁻¹ h⁻¹), at (a) 1600, (b) 1745, (c) 1915, (d) 2030, (e) 2145, and (f) 2354 UTC. Horizontal wind vectors at the lowest grid level also appear (the tail of each vector is located at every 20th grid point), and their length is scaled by the wind speed. The objectively determined positions of the front have been overlaid as in Fig. 10. The locations of the dual-Doppler wind synthesis domains can be viewed in Figs. 2 and 5.

ential diabatic heating has been neglected and tilting is nearly zero at the lowest grid level.

At the start of the deployment, the front was ill defined in the vertical velocity field (Fig. 10a). The largest vertical velocities were observed within horizontal convective rolls (HCRs) on the warm (south) side of the front (3 m s^{-1} at 750 m, versus $\sim 2 \text{ m s}^{-1}$ along the front at the same altitude). The HCRs were oriented approximately parallel to the boundary layer winds and mean shear. The vertical motions along the front became better defined along the front in time. Between 1557 and 1745 UTC, S increased from 0.75 to 0.95 (Fig. 13). Peak vertical velocities along the front (w_{max}) also increased in time, reaching 3 m s^{-1} by the end of the deployment (Figs. 10b and 13).

The largest vertical vorticity values were observed along the front (Fig. 10). We will refer to these vorticity extrema as vortices, with the acknowledgment that vortices can be difficult to define objectively (Lugt 1979).⁴ The peak vertical vorticity along the front (ζ_{max}) ranged from 0.008 to 0.014 s^{-1} , with ζ_{max} increasing in time from 1557 to 1745 UTC, and then declining slightly thereafter (Fig. 13). The fact that the strongest vortices were confined to the front, during this deployment as well as the other three deployments, suggests that horizontal shearing instability was important for their development. However, the spacing between vortices (wavelength) was highly irregular and therefore difficult to define (e.g., Fig. 10b). In several previous studies (e.g., Carbone 1982; Wakimoto and Bosart 2000), vortices were fairly regularly spaced, with a wavelength approximately 7.5 times the width of the zone of horizontal shear, which is the most unstable wavelength for horizontal shearing instability (Haurwitz 1949; Miles and Howard 1964).

The magnitude of the horizontal vorticity was much larger on the cold (north) side of the front compared with the warm (south) side (Figs. 15a,b), presumably because this is where baroclinic generation of horizontal vorticity was largest (Fig. 12). The horizontal vorticity had a large alongfront component, as would be expected to be the case given the orientation of the density gradient. The maximum magnitude of the 0–1-km mean horizontal vorticity within 5 km of the front ($|\overline{\omega}_h|_{\text{max}}$) increased throughout deployment 1, from $\sim 0.009 \text{ s}^{-1}$ at 1557 UTC to $>0.011 \text{ s}^{-1}$ at 1818 UTC (Fig. 13).

The tendency of Γ_v and Γ_h might present a more representative perspective on the evolution of the ver-

tical and horizontal vorticity fields than either ζ_{max} or $|\overline{\omega}_h|_{\text{max}}$. Both Γ_v and Γ_h increased during deployment 1 (Fig. 13), just as ζ_{max} and $|\overline{\omega}_h|_{\text{max}}$ increased. Because changes in Γ_h can be accomplished by baroclinic generation of circulation within a vertical cross section (in addition to advection), one might expect that increases in $|\overline{\omega}_h|_{\text{max}}$ —which also is strongly influenced by baroclinic generation—should be matched reasonably well by increases in Γ_h , as was observed (both increased by $\sim 20\%$ during the 1557–1745 UTC period). On the other hand, the increase of Γ_v was relatively small ($\sim 10\%$) compared with the increase of ζ_{max} ($\sim 40\%$) during the 1557–1745 UTC period. This might not be surprising since three-dimensional effects (e.g., stretching) are known to have an important influence on boundary layer vortices, even those whose origins are (two-dimensional) horizontal shearing instability (e.g., Lee and Wilhelmson 1997). Changes in Γ_v are largely due to the flux of Coriolis rotation into or out of the region defined by the circuit (Fig. 9) and advection (baroclinic generation of Γ_v is very small)—changes in the strength of vortices due to stretching do not alter Γ_v . Thus, one might expect that changes in ζ_{max} would not necessarily be closely matched by changes in Γ_v .

In summary, the baroclinity associated with the front increased throughout most of deployment 1 (until approximately 1745 UTC), as did the slabularity, vertical velocity, vertical vorticity and circulation, horizontal vorticity and circulation, and deformation along the front. Between 1745 and 1800 UTC, the baroclinity, slabularity, vertical vorticity and circulation, horizontal circulation, and deformation began to weaken, and this weakening continued through the end of deployment 1 and through deployment 2. Deployment 1 was terminated at 1818 UTC in order to reposition the radars to accommodate the southward motion of the front out of the dual-Doppler domain.

c. Deployment 2: 1910–2033 UTC

By the time dual-Doppler data collection resumed at 1910 UTC, the baroclinity along the front had decreased dramatically (Figs. 12c and 13). From the end of deployment 1 to the start of deployment 2, $|\partial\theta_v/\partial n|$ dropped from $3.1 \text{ K (10 km)}^{-1}$ to $0.9 \text{ K (10 km)}^{-1}$. Although the domain in which surface observations were obtained shifted between deployments 1 and 2 (Fig. 5), it is unlikely that the relatively small shift in the location of the domain ($\sim 10 \text{ km}$ southward) can explain such a large change in the observed baroclinity.

The strength of the baroclinity continued to weaken throughout deployment 2, such that $|\partial\theta_v/\partial n|$ fell to $0.2 \text{ K (10 km)}^{-1}$ by the end of deployment 2 (2033 UTC; Figs. 12d and 13). Not surprisingly, the horizontal vor-

⁴ Popular definitions of vortices often require closed streamlines or local vorticity anomalies, but even these definitions can have significant limitations (Lugt 1979).

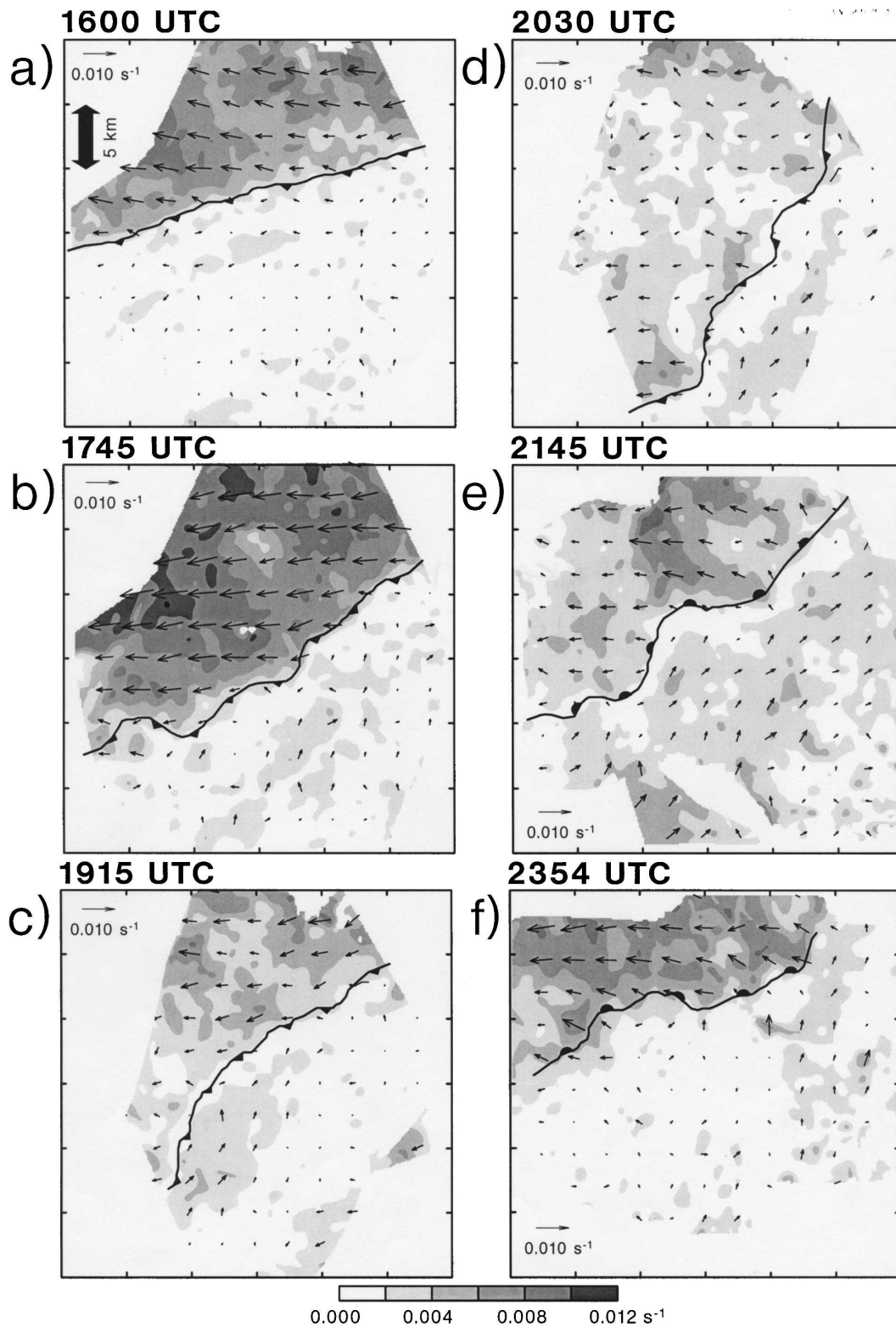


FIG. 15. Horizontal cross sections of the magnitude of the mean 0–1-km horizontal vorticity (shaded) at (a) 1600, (b) 1745, (c) 1915, (d) 2030, (e) 2145, and (f) 2354 UTC. The mean horizontal vorticity vectors also appear (the tail of each vector is located at every 20th grid point), and their length is scaled by the magnitude of the horizontal vorticity. The objectively determined positions of the front have been overlaid as in Fig. 10. The locations of the dual-Doppler wind synthesis domains can be viewed in Figs. 2 and 5.

ticity on the cold side of the front also was diminished significantly compared with deployment 1 (Figs. 15c,d), as was Γ_h (Fig. 13). Throughout deployment 2, positive, albeit weak, frontogenetic forcing was observed along the front despite weakening deformation (Figs. 14c,d). One must therefore conclude that the weakening baroclinity was brought about by frontolytic differential diabatic heating, as is commonly the case when the primary diabatic effect is the surface sensible heat flux, which is larger in the cold air mass.

The motion of the front slowed throughout deployment 2, perhaps in response to the weakening density gradient across the front. The southward motion of the front slowed from approximately 3 m s^{-1} at the beginning of the deployment (1910 UTC) to $1\text{--}2 \text{ m s}^{-1}$ at the end of the deployment (2033 UTC). Just as the increase in $|\partial\theta_v/\partial n|$ in deployment 1 was closely accompanied by an increase in S , the decrease in $|\partial\theta_v/\partial n|$ in deployment 2 was accompanied by a decrease in S . From 1910 to 2033 UTC, S decreased from 0.92 to 0.74, although w_{max} remained fairly constant at approximately 3 m s^{-1} (Figs. 10c,d and 13).

Despite the weakening of the front that occurred after approximately 1745 UTC, at least in terms of its baroclinity, slabularity, and horizontal circulation (which probably can be regarded as a measure of the strength of the frontal dynamics), prominent vertical vortices continued to be observed along the front throughout deployment 2 (Figs. 10c,d and 13). In fact, the strongest vortices observed were observed near the start of deployment 2 (1910 UTC; Fig. 10c), with a ζ_{max} of approximately 0.015 s^{-1} . The radar reflectivity fine line associated with the front displayed numerous lobes and clefts throughout the deployment. The strongest vortices were associated with fine line structures that resembled breaking waves (Fig. 16), similar to those documented by Carbone (1982), Marquis (2005), and Young et al. (2005), among others. The vortices also tended to be located within vertical velocity relative minima (Fig. 17), which is likely a result of downward-directed dynamic pressure gradients within the vortices owing to the fact that rotation tends to decrease with height within them (Markowski and Hannon 2006). In other words, the vortices are closely related to “fractures” in the vertical velocity field, as also have been documented in numerous prior studies (e.g., Carbone 1982; Parsons and Hobbs 1983; Moore 1985; Braun et al. 1997). In section 5 we will comment further on the possible dynamical linkages between the vertical velocity and vertical vorticity fields and the slabularity.

It may be noteworthy that the reflectivity fine line was virtually always unbroken, even when slabularities significantly less than unity were observed (e.g., Fig.

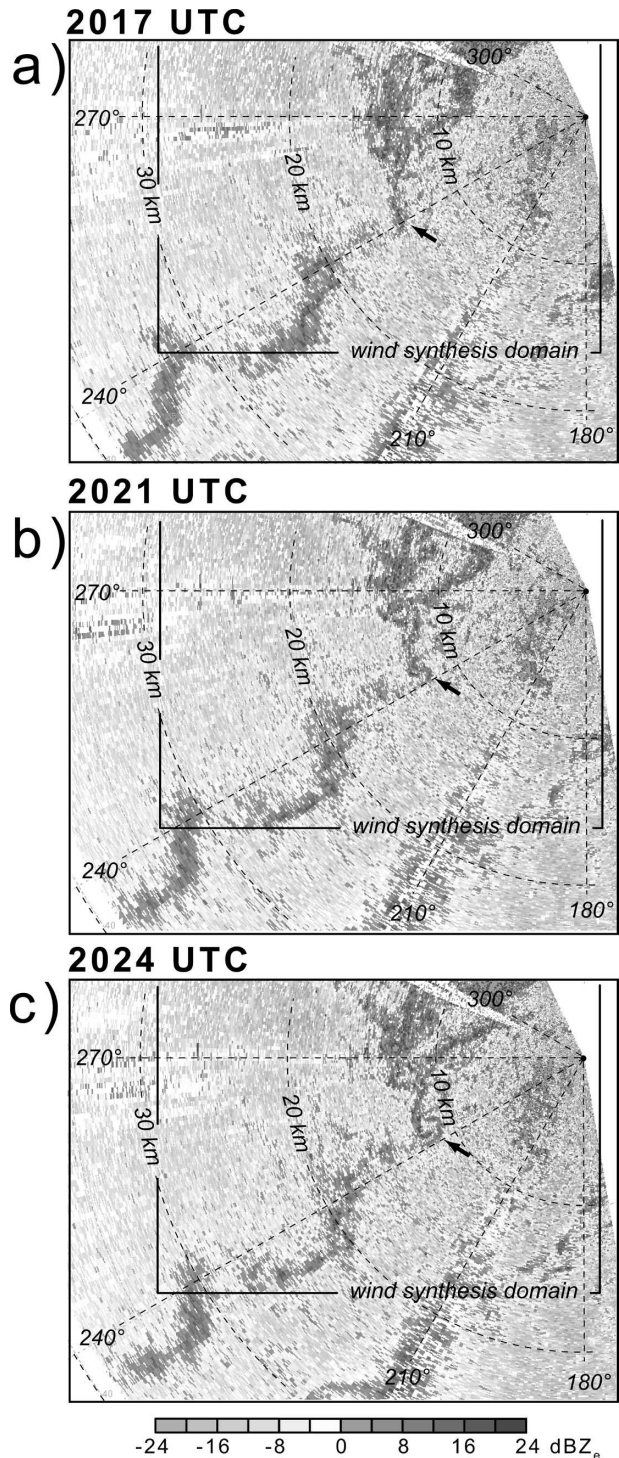


FIG. 16. Equivalent radar reflectivity factor from the DOW2 radar at (a) 2017, (b) 2021, and (c) 2024 UTC. The arrow indicates the location of a breaking wave along the reflectivity fine line associated with the front (see text for further discussion). The wind synthesis domain displayed in Figs. 10c,d, 12c,d, 14c,d, and 15c,d is also indicated.

2000 UTC

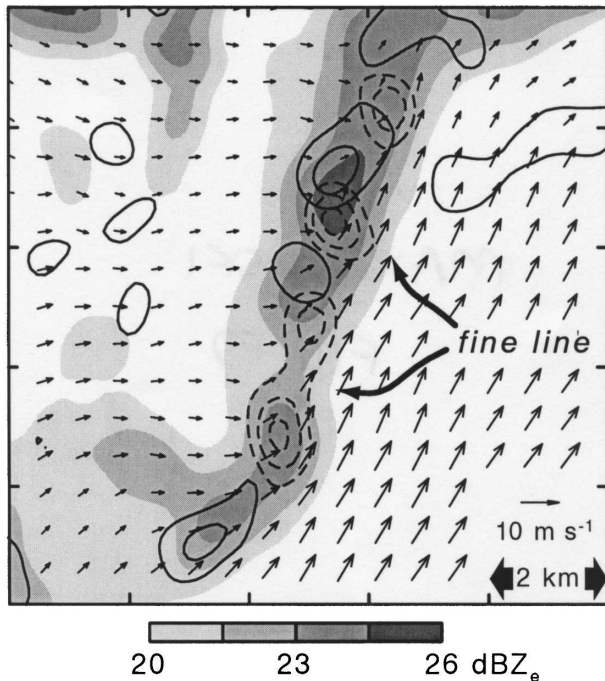


FIG. 17. Horizontal cross section showing objectively analyzed equivalent radar reflectivity factor at 750 m (shaded), updraft maxima at 750 m (solid contours are drawn every 1 m s^{-1} , starting at 1 m s^{-1}), and vorticity maxima at the lowest grid level (solid contours are drawn every $2.5 \times 10^{-3} \text{ s}^{-1}$, starting at $5.0 \times 10^{-3} \text{ s}^{-1}$) at 2000 UTC in a $10 \text{ km} \times 10 \text{ km}$ subdomain of the domain displayed in Figs. 10c,d, 12c,d, 14c,d, and 15c,d. Horizontal wind vectors at the lowest grid level also are drawn (the tail of each vector is located at every 5th grid point), and their length is scaled by the wind speed.

17). Because the reflectivity fine line that is commonly collocated with a convergent mesoscale boundary is assumed to be a manifestation of insect lofting by the mesoscale updraft, one might have expected that a reflectivity fine line would have a pattern nearly identical to the vertical velocity field. Instead, the linear correlation between radar reflectivity and vertical velocity was observed to be only 0.4–0.6, depending on the analysis time and elevation. B. Geerts (2004, personal communication) has observed similar correlations using the Wyoming cloud radar (95 GHz). It seems likely that the fine line would be better correlated with vertical displacements [i.e., the reflectivity composing the fine line (the insects) should be better related to the *history* of ascent than the instantaneous ascent rate].

d. Deployment 3: 2112–2233 UTC

Approximately 40 min elapsed between the end of deployment 2 and the start of deployment 3, during which time the mobile radars were repositioned ap-

proximately 30 km to the northeast (Fig. 5). The winds throughout the boundary layer accelerated toward the northwest between 2030 and 2145 UTC on both sides of the front, resulting in strong ($\geq 10 \text{ m s}^{-1}$) southerly winds (previously southwesterly) south of the front and very light (approximately $1\text{--}2 \text{ m s}^{-1}$) south-to-southwesterly winds north of the front (Fig. 10e). The slow southward motion of the front observed at the conclusion of deployment 2 was now reversed (Fig. 5). The northward motion of the front increased in time, such that it was moving at $\sim 5 \text{ m s}^{-1}$ by the time it exited the dual-Doppler domain to the north at 2215 UTC.⁵

The baroclinity associated with the front (now a warm front) slowly increased throughout deployment 3; $|\partial\theta_v/\partial n|$ increased from 0.2 to $0.5 \text{ K (10 km)}^{-1}$ between 2112 and 2215 UTC (Figs. 12e and 13), as did the deformation and scalar frontogenesis (Fig. 14e). The horizontal vorticity within the warm sector away from the front increased between deployments 2 and 3, as did the horizontal vorticity on the cold side of the front; thus, the front was situated near a well-defined relative minimum in horizontal vorticity (Fig. 15e). Observations of w_{max} were larger during deployment 3 than in the previous deployments, with values approaching 3.5 m s^{-1} (Figs. 10e and 13). The slabularity also generally followed the trend in $|\partial\theta_v/\partial n|$, ranging from roughly 0.78–0.90 during deployment 3, with a brief maximum near 2200 UTC coincident with a maximum in $|\partial\theta_v/\partial n|$ of 0.7 K km^{-1} at the same time (Fig. 13).

The intensity of the vertical vortices along the front was similar to the intensity near the conclusion of deployment 2. The strongest vortices ($\zeta_{\text{max}} \sim 0.012 \text{ s}^{-1}$) were associated with fractures in the vertical velocity field (not shown) similar to those described in section 4c. Curiously, Γ_v decreased markedly (by $\sim 50\%$) between 2112 and 2215 UTC, yet ζ_{max} exhibited no such decrease.

e. Deployment 4: 2339–0000 UTC

The front continued to accelerate northward after deployment 3, to speeds exceeding 10 m s^{-1} by 2330 UTC. Given the rapid motion of the front, it was extremely difficult to continue mobile radar operations. After slightly more than an hour of “chasing” the front northward, a brief, final deployment was undertaken from 2339–0000 UTC, approximately 40 km north-northeast of the location of deployment 3 (Fig. 5).

⁵ Although the front exited the dual-Doppler domain at 2215 UTC, data collection continued until 2233 UTC because it was not known in real time that the front had exited the dual-Doppler domain 18 min earlier.

Winds south of the front accelerated to speeds in excess of 15 m s^{-1} at the lowest grid level by 0000 UTC. The baroclinity was significantly larger compared with that observed in deployments 2 and 3 by the time the mobile mesonet was able to resample the front farther north; $|\partial\theta_v/\partial n|$ was $\sim 1.3 \text{ K (10 km)}^{-1}$ (Figs. 12f and 13). The deformation, which continued to be frontogenetic as in earlier deployments, also increased (Fig. 14f) relative to deployments 2 and 3 (perhaps the net increase in the baroclinity between deployments 3 and 4 was a result of a decrease in frontolytic differential diabatic heating). Likewise, $|\overline{\omega}_h|_{\max}$, Γ_h , and w_{\max} increased as well (Figs. 13 and 15f). Values of ζ_{\max} and Γ_v in deployment 4 were similar to the peak values occurring in deployment 3 (Figs. 10f and 13). Perhaps curiously, S decreased to its lowest values (<0.75) since the beginning of deployment 1, despite the increasing baroclinity.

5. Discussion of possible implications for convection initiation

As indicated in section 1, the data collection occurred in conjunction with the convection initiation component of IHOP. CIN was exceptionally large in this case, so much so that even shallow cumulus clouds were prohibited. Given the overwhelmingly unfavorable large-scale conditions, it is not clear how one might evaluate the importance of finescale dynamical processes associated with the front in the initiation or suppression of deep convection, *in this particular case*. However, even though the reasons for the failure of convection to be initiated along the cold front seem rather obvious in this case, it is possible that the observations made in this study could have implications for convection initiation in other cases in which the large-scale environment is less hostile.

The initiation of deep, moist convection requires that parcels of air reach their LFC and achieve positive buoyancy, and then maintain positive buoyancy over a significant upward vertical excursion. One of the complexities of convection initiation arises from the fact that entrainment, which tends to reduce buoyancy and potential buoyancy, occurs within air parcels en route to the lifting condensation level (LCL) and LFC (and beyond). Thus, convection initiation is not as simple as reaching the so-called “convective temperature” or reducing CIN to zero. CIN calculations, at best, can only crudely account for mixing en route to the LCL and LFC (typically this is done by lifting a parcel of air having the mean potential temperature and specific humidity over part or all of the boundary layer depth).

Because overcoming the effects of entrainment is so crucial, one might naturally consider both the tilt of the frontal updraft and the slabularity of the front to be pertinent to convection initiation. As the tilt of the frontal updraft increases, one would expect the dilution of equivalent potential temperature θ_e , which describes the potential buoyancy of an air parcel that may be realized above the LFC, to increase as a result of increased mixing (Weisman 1992). However, increases in slabularity might be expected to reduce the amount of θ_e dilution by reducing the exposure of the ascending plumes of potentially buoyant air to the ambient, hostile environment, in which θ_e tends to decrease with height.

The potential importance of updraft tilt in convection initiation suggests some applicability of the theory presented by Rotunno et al. (1988), which relates the slope of the updraft along the leading edge of a density current to the magnitudes of the density excess and ambient wind shear. Figure 18 presents vertical cross sections of front-relative streamlines normal to the front through the maximum frontal updraft. An approximately inverse relationship is evident between the slope of the ascent over the front and the baroclinity associated with the front,⁶ as would be predicted by Rotunno et al., given the weak warm sector shear normal to the front (and overall). For example, at 1745 UTC, the time at which $|\partial\theta_v/\partial n|$ is a maximum, the frontal updraft is most inclined from the vertical. Conversely, at 2030 UTC, the time at which $|\partial\theta_v/\partial n|$ is a minimum, the frontal updraft is nearly erect. Also note the horizontal vorticity vectors on either side of the front at this time (Fig. 15d) are nearly equal in magnitude and opposite in direction, generally speaking, implying the sort of balance advocated by Rotunno et al. (1988).

Although the tilt of the frontal updraft increased with increasing baroclinity, the slabularity also increased with increasing baroclinity. The relationship among slabularity, updraft tilt, and θ_e dilution via mixing is therefore unclear. A frontal updraft that is significantly tilted away from the vertical might have a reduced probability of convection initiation following Rotunno et al.’s (1988) reasoning, but large slabularity, which tends to be accompanied by large updraft tilt, might enhance the probability of convection initiation if quasi-two-dimensional frontal updrafts are less prone to θ_e dilution than three-dimensional updrafts surrounded on all

⁶ This relationship might be anticipated from Margules’s equation (Palmen and Newton 1969, 168–173), although Margules’s equation strictly applies only to the slope of an interface separating homogeneous air masses in steady geostrophic motion parallel to the interface.

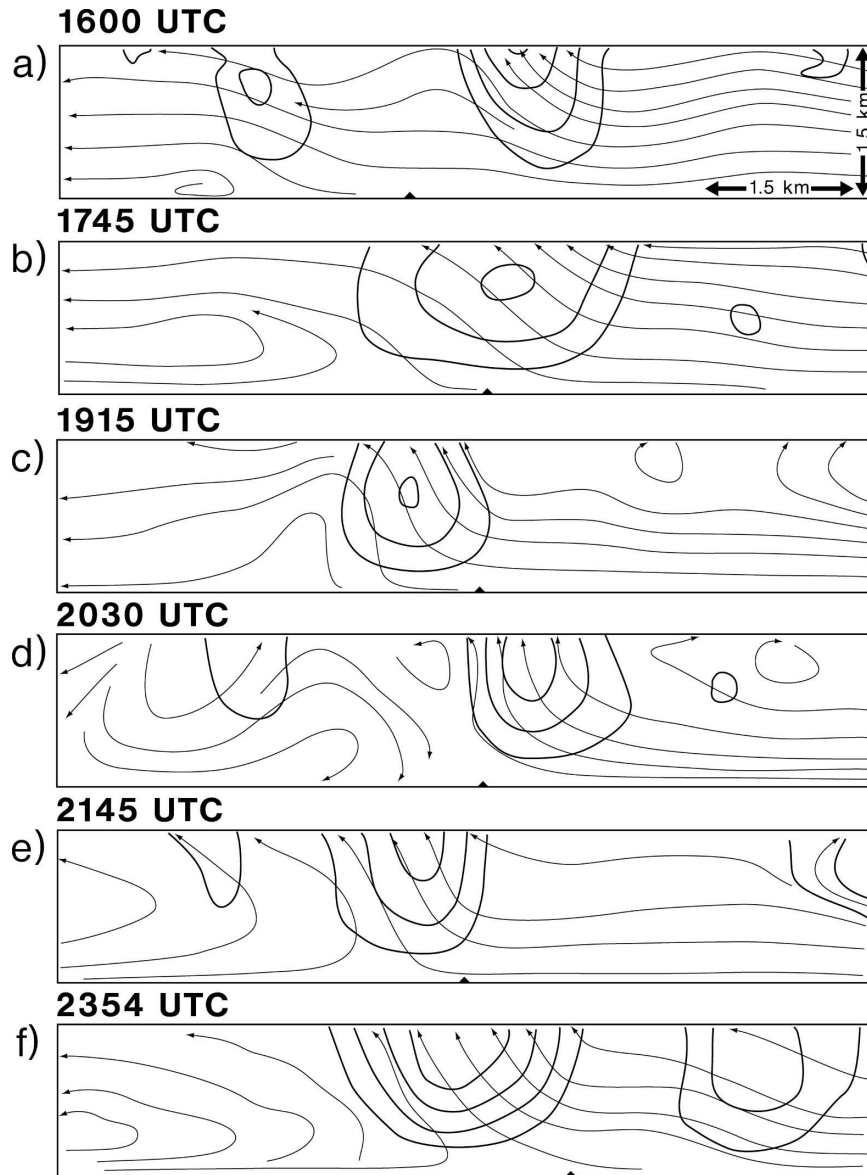


FIG. 18. Vertical cross sections of front-relative streamlines at (a) 1600, (b) 1745, (c) 1915, (d) 2030, (e) 2145, and (f) 2354 UTC. Vertical velocity contours of 1, 2, 3, and 4 m s^{-1} are overlaid. The locations of the cross sections are indicated in Fig. 10. Cold air to the left in (a)–(f). The intersection of each cross section with the front at the surface is indicated with a triangular marker at the bottom of (a)–(f).

sides by ambient air. On the other hand, the relationship between the tilt of the frontal updraft and the baroclinity associated with the front probably is case dependent, because the tilt likely also depends on the warm sector horizontal vorticity (Rotunno et al. 1988).

Although the slabularity is strongly influenced by the relative importance of the thermally direct frontal circulation compared with the motions induced by boundary layer convection (Fig. 11), the time series of $|\partial\theta_v/\partial n|$, Γ_h , and S (Fig. 13) indicates that the slabularity

depends on more than simply the strength of the thermally direct frontal circulation (and associated baroclinity). Throughout deployment 1 (1557–1818 UTC), the increase in $|\partial\theta_v/\partial n|$ and Γ_h was closely matched by an increase in S (Fig. 13), similar to observations made by Arnott et al. (2006) in another IHOP case. But at the start of deployment 2 (1910 UTC), Γ_h and $|\partial\theta_v/\partial n|$ were significantly smaller than at the conclusion of deployment 1, yet S remained relatively large (Fig. 13). Eventually S decreased during deployment 2, but it is appar-

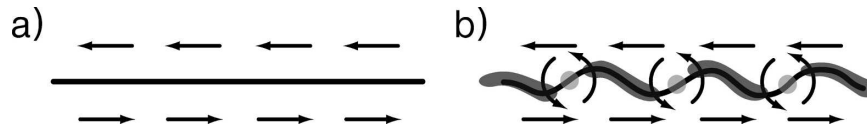


FIG. 19. (a) Schematic depiction of a boundary separating two air masses (indicated by the solid line), along which there is a wind shift but no convergence; thus, the vertical motion is zero everywhere. (b) If the boundary is perturbed and the horizontal wind shear along the boundary gives rise to vortices, vertical velocity maxima (dark gray), and minima (light gray) arise between the vortices and near the centers of the vortices, respectively. If the slabularity is initially zero, as in (a), the vortices in (b) lead to an increase in slabularity. If the boundary is initially convergent with little along-boundary heterogeneity in the wind such that the slabularity is large (not shown), then the development of vortices such as in (b) leads to a reduction in slabularity. See text for further details.

ent that S depends on more than just the strength of the thermally direct frontal circulation. One possibility is that the presence of strong vortices along the front helped to maintain the slabularity even as the baroclinity weakened. The intensity of the vortices increased markedly in the second half of deployment 1 (after ~ 1715 UTC), and ζ_{\max} remained relatively large (generally $>0.011 \text{ s}^{-1}$), at least compared with the first half of deployment 1, throughout deployments 2, 3, and 4.

The influence of vortices on slabularity is perhaps not as intuitive as the influence of the thermally direct frontal circulation. Consider a boundary separating two air masses, along which there is a wind shift but no convergence, and all of the vorticity lies along the interface separating the two air masses (a vortex sheet may be present, or the wind shift corridor may have a finite width; Fig. 19a). Because there is no convergence along the boundary, there is no vertical motion, and thus the slabularity is zero. Now suppose that the corridor of large horizontal wind shear along the boundary separating the air masses is perturbed, such that shearing instability results in the formation of several vortices along the boundary (Fig. 19b). The superpositioning of the initial wind field and motions associated with the vortices results in horizontal convergence between the vortices, as has been shown by Marquis et al. (2004), Marquis (2005), and Xue and Martin (2006). Because the low-level horizontal convergence is necessarily associated with updrafts, the slabularity is increased from its initial value of zero. On the other hand, because the rotation within boundary layer vortices tends to weaken with height, the cores of vortices have been shown to be associated with downward-directed dynamic pressure gradient forces, and even downdrafts (e.g., Markowski and Hannon 2006). Thus, a boundary having initially large slabularity and few and/or weak vortices may have its slabularity reduced by an increase in the number and/or intensification of the vortices (Fig. 19b). Arnott et al. (2006) documented a similar evolution.

In summary, the time series of $|\overline{\partial\theta_v/\partial n}|$, Γ_h , ζ_{\max} , and S (Fig. 13) suggest that slabularity is a complex function of the thermally direct frontal circulation and vortices. In the absence of numerous, strong vortices, slabularity increases as the thermally direct frontal circulation increases (Fig. 11). If strong vortices arise along a front, slabularity can be either reduced or enhanced, depending on the slabularity that would be associated with the front in the absence of vortices (Fig. 19). One additional complication worth mentioning is the good possibility that the number and strength of vortices themselves might be related to baroclinity and strength of the frontal circulation, at least indirectly (e.g., the horizontal shear across a front should depend somewhat on the baroclinity, and the horizontal shear might exert some influence on the number and strength of the vortices, at least if horizontal shearing instability is playing a role).

Finally, in addition to the possible relevance of slabularity to convection initiation in terms of the “protection” of ascending plumes of potentially buoyant air, the slabularity of a mesoscale boundary might influence the *mode* of the convection that is initiated (e.g., discrete cells versus a squall line). In idealized numerical simulations, identical environments can support either isolated supercells or severe squall lines—the only difference is how the convection is initiated. For example, to obtain an isolated supercell, convection typically is triggered by the introduction of a single warm bubble (e.g., Klemp and Wilhelmson 1978), whereas squall-line formation typically is instigated by the introduction of an infinitely long warm bubble (e.g., Weisman et al. 1988) or a series of warm bubbles aligned in a row (e.g., Weisman and Trapp 2003). In other words, the mode of convection organization depends strongly on how the convection is initiated. Based on the aforementioned techniques of initiating various forms of convection in a numerical model, one might hypothesize that a mesoscale boundary having large slabularity would be more prone to initiate a squall line, whereas a mesoscale

boundary having small slabularity might be more prone to initiate isolated thunderstorms.

6. Summary, conclusions, and future work

Three-dimensional wind syntheses derived from dual-Doppler radar observations were used to document the kinematic structure of a front for nearly 5.5 h of the 1557–0000 UTC period on 3 June 2002 during IHOP. During the first mobile radar deployment (1557–1818 UTC), the front moved slowly southward as a cold front. The baroclinity associated with the front, as determined by analyses of mobile mesonet data, increased substantially between 1557 and 1745 UTC [$|\partial\theta_v/\partial n|$ increased from 1.8 to 3.7 K (10 km) $^{-1}$], apparently as a result of frontogenetic deformation. The increase in baroclinity was followed by a slight decrease during the remainder of the first deployment. The increases in baroclinity were accompanied by an increase in the thermally direct frontal circulation, as well as the alongfront contiguity of the frontal updraft, that is, the slabularity (S increased from 0.75 to 0.95 between 1557 and 1745 UTC). The increase in horizontal wind shear across the front throughout the first deployment was accompanied by an increase in the intensity of vertical vortices along the front (ζ_{\max} increased from ~ 0.009 to ~ 0.014 s $^{-1}$ between 1557 and 1745 UTC).

Between the first and second deployments, the baroclinity associated with the front decreased dramatically [$|\partial\theta_v/\partial n|$ decreased to 0.9 K (10 km) $^{-1}$], presumably due to differential diabatic heating, because the deformation along the front was still frontogenetic. The baroclinity continued to decline throughout the second deployment (1910–2033 UTC), such that by the end of the deployment, only a negligible density gradient was observed across the front [$|\partial\theta_v/\partial n|$ of approximately 0.2 K (10 km) $^{-1}$]. Not surprisingly, the thermally direct frontal circulation was much weaker in the second deployment. The intensity of the vertical vortices also waned somewhat, but their intensity still remained rather high compared with the first half of deployment 1 (ζ_{\max} decreased from 0.015 to 0.011 s $^{-1}$). The slabularity of the front decreased throughout the second deployment (S decreased to ~ 0.70 by 2033 UTC), although the slabularity remained very high (>0.90) at the start of the deployment despite the baroclinity being substantially weaker at that time compared with any time within deployment 1. Thus, during the second deployment, the relationship between the baroclinity and slabularity was not as strong as the relationship between baroclinity and the thermally direct frontal circulation. By the end of the second deployment, the front had nearly stalled, perhaps as a result of the weakening density differential

across the front in addition to larger-scale influences, which were inducing northwestward wind accelerations over the entire region.

During the third and fourth deployments of the mobile radars (2112–2233 and 2339–0000 UTC), the front moved northward as a warm front, its speed increasing in time. The baroclinity gradually increased in time as well, although it never became as strong as during the second half of the first deployment (~ 1745 UTC). The thermally direct frontal circulation likewise intensified, and strong vertical vortices (>0.012 s $^{-1}$) continued to be observed along the front on occasion. It is not possible to generalize the tendency of the slabularity during these deployments—it did not closely follow the trend in the baroclinity.

The conclusions that can be extracted from this study are summarized below.

- Vertical vortices were strongest when the horizontal wind shear across the front was largest, suggesting that shearing instability played a role in the genesis and/or intensification of the vortices; however, in contrast to many previous studies, the spacing between vortices was highly irregular.
- When vertical vortices along the front were relatively weak, slabularity increased with the strength of the thermally direct frontal circulation (which closely responded to changes in the front-normal density gradient, as expected); therefore, during these times, slabularity was a good measure of the relative contribution to the vertical motion field from the frontal circulation compared with the contribution from boundary layer convection.
- When vertical vortices were relatively strong, it was difficult to generalize the relationship between slabularity and the strength of the thermally direct frontal circulation because of the ways by which strong vortices may influence the vertical velocity field, and thus slabularity.

It is hypothesized that the slabularity of a mesoscale boundary might influence the organization of the convection that is initiated (e.g., discrete cells versus solid lines). It also is possible that the slabularity of a mesoscale boundary might be relevant to the initiation of deep convection by reducing the exposure of ascending plumes of potentially buoyant air to the ambient, hostile environment, in which θ_e tends to decrease with height. On the other hand, periods of large slabularity were also frequently observed when the frontal updraft was significantly tilted away from the vertical—at these times, the strong thermally direct frontal circulation that was promoting the large slabularity was also tilting the frontal updraft over the cold air. Future work might

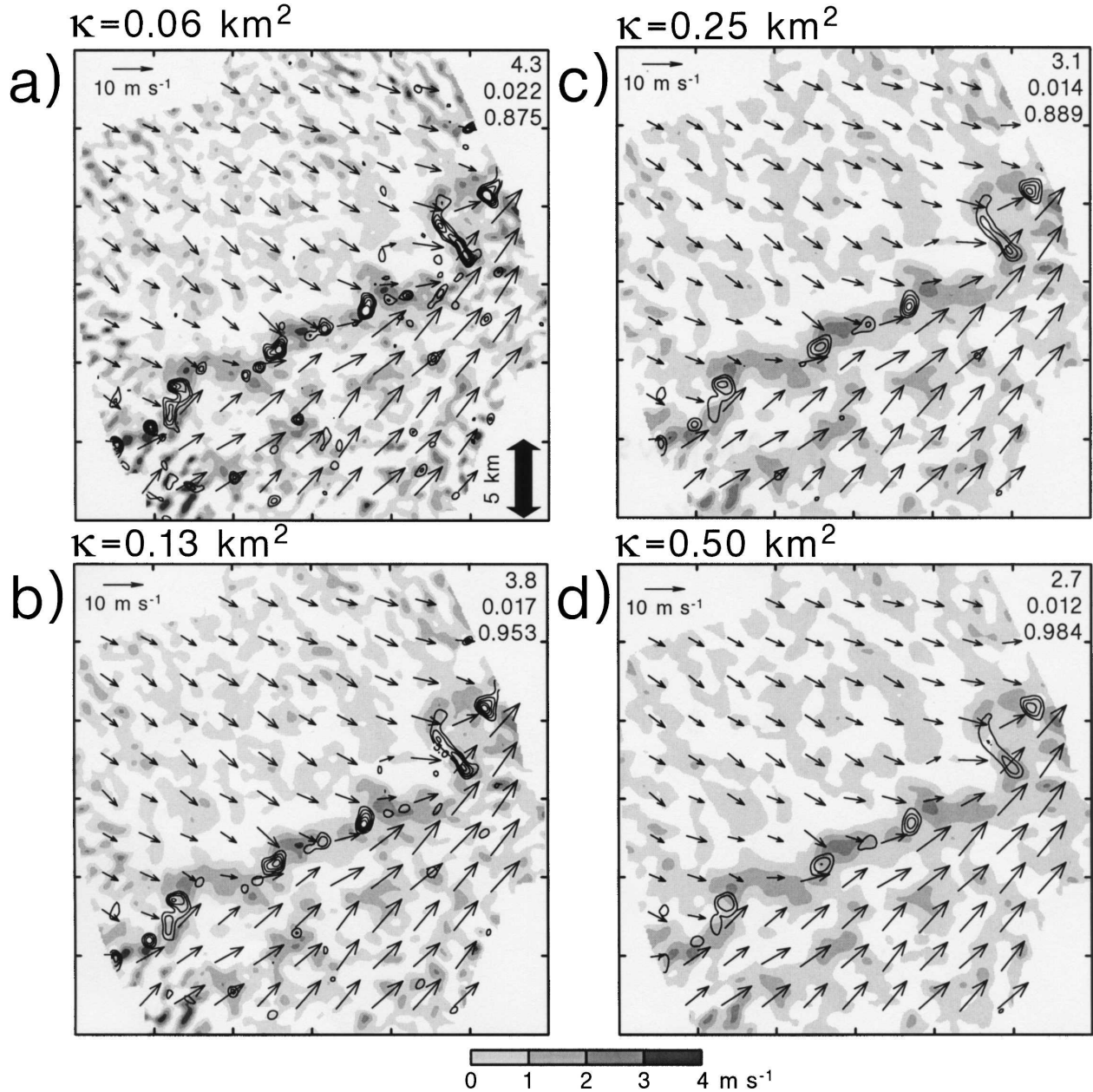


FIG. A1. Horizontal cross sections showing regions of updraft at 750 m (shaded) and vorticity maxima at the lowest grid level (solid contours are drawn every $2.5 \times 10^{-3} \text{ s}^{-1}$, starting at $5.0 \times 10^{-3} \text{ s}^{-1}$) at 1800 UTC using a Barnes smoothing parameter κ of (a) 0.06, (b) 0.13, (c) 0.25, and (d) 0.50 km^2 . Horizontal wind vectors at the lowest grid level are also shown.

explore the importance of slabularity versus updraft tilt in reducing θ_e dilution within ascending plumes of air en route to the LFC. What is also evident from a growing number of studies, this one included, is that vertical vortices can significantly modulate the vertical motion field along mesoscale boundaries, and the development of the vortices themselves likely depend on the characteristics of the mesoscale boundary. We believe that further study of the conditions in which strong vortices

might arise, the complex processes by which vortices may merge or are maintained, and the feedbacks between the vertical velocity and vorticity fields is well warranted.

Acknowledgments. We are grateful to Drs. Yvette Richardson, Josh Wurman, George Young, Erik Rasmussen, and Conrad Ziegler for their constructive suggestions throughout the course of this work. We also

thank all of the IHOP planners and volunteers who facilitated the collection of the data relied upon for this study, particularly Drs. Tammy Weckwerth and David Parsons. We also thank the two anonymous reviewers who pointed out several areas in which the presentation could be clarified. This research was supported by National Science Foundation Grant ATM-0130307 made to the Pennsylvania State University.

APPENDIX

Sensitivity of the Wind Syntheses to the Specification of the Barnes Smoothing Parameter

In this appendix we explore the sensitivity of the three-dimensional wind syntheses on the Barnes smoothing parameter κ . Objective analyses were produced using a range of smoothing parameters, equal to one-quarter (0.062 km^2), one-half (0.13 km^2), and twice (0.50 km^2) the magnitude of the smoothing parameter used in the synthesis of the three-dimensional wind fields shown in Figs. 10, 14, and 15. The wind syntheses obtained using this range of κ values are presented at 1800 UTC in Fig. A1, which displays vertical velocity and vertical vorticity in a manner similar to that in Fig. 10. The maximum vertical velocity (vertical vorticity) values within the domain vary from 2.7 to 4.3 m s^{-1} ($0.012\text{--}0.022 \text{ s}^{-1}$), with the amplitudes of the vertical velocity and vorticity extrema increasing with decreasing κ . Not surprisingly, the slabularity is also sensitive to κ , with slabularity increasing with decreasing κ . Although the details of the three-dimensional wind synthesis are fairly sensitive to κ , the fields are qualitatively similar. The temporal evolution of the fields also is qualitatively the same regardless of κ . Thus, the conclusions presented in section 6 are unaffected by the choice of κ .

The sensitivity of the objectively analyzed radial velocities and three-dimensional wind syntheses to other parameters involved in the radar data analysis (e.g., the cutoff radius of the Barnes objective analysis, advection velocity, and azimuth correction) has also been explored, but is not included here in the interest of brevity. In general, the sensitivities are not as large as the sensitivity to κ . For an analysis and discussion of these effects, the reader is referred to Markowski et al. (2006).

REFERENCES

- Arnott, N., Y. Richardson, J. Wurman, and J. Lutz, 2003: A solar calibration technique for determining mobile radar pointing angles. Preprints, *31st Conf. on Radar Meteorology*, Seattle, WA, Amer. Meteor. Soc., 492–494.
- , —, —, and E. N. Rasmussen, 2006: Relationship between a weakening cold front, mesocyclones, and cloud development on 10 June 2002 during IHOP. *Mon. Wea. Rev.*, **134**, 310–334.
- Barnes, S. L., 1964: A technique for maximizing details in numerical weather map analysis. *J. Appl. Meteor.*, **3**, 396–409.
- Biggerstaff, M. I., and Coauthors, 2005: The Shared Mobile Atmospheric Research and Teaching Radar: A collaboration to enhance research and teaching. *Bull. Amer. Meteor. Soc.*, **86**, 1263–1274.
- Braun, S. A., R. A. Houze Jr., and B. F. Smull, 1997: Airborne dual-Doppler observations of an intense frontal system approaching the Pacific Northwest coast. *Mon. Wea. Rev.*, **125**, 3131–3156.
- Buban, M. S., C. L. Ziegler, and E. N. Rasmussen, 2003: The kinematic and thermodynamic effects of vortices within a dryline. Preprints, *31st Conf. on Radar Meteorology*, Seattle, WA, Amer. Meteor. Soc., 789–792.
- Carbone, R. E., 1982: A severe frontal rainband. Part I: Stormwide hydrodynamic structure. *J. Atmos. Sci.*, **39**, 258–279.
- Clarke, R. H., 1961: Mesostucture of dry cold fronts over featureless terrain. *J. Meteor.*, **18**, 715–735.
- Gal-Chen, T., 1978: A method for the initialization of the anelastic equations: Implications for matching models with observations. *Mon. Wea. Rev.*, **106**, 587–606.
- Hane, C. E., and P. S. Ray, 1985: Pressure and buoyancy fields derived from Doppler radar data in a tornadic thunderstorm. *J. Atmos. Sci.*, **42**, 18–35.
- Haurwitz, B., 1949: The instability of wind discontinuities and shear zones in planetary atmospheres. *J. Meteor.*, **6**, 200–206.
- Hobbs, P. V., and K. R. Biswas, 1979: The cellular structure of narrow cold-frontal rainbands. *Quart. J. Roy. Meteor. Soc.*, **105**, 723–727.
- , and P. O. G. Persson, 1982: The mesoscale and microscale structure and organization of clouds and precipitation in mid-latitude cyclones. Part V: The substructure of narrow cold frontal rainbands. *J. Atmos. Sci.*, **39**, 280–295.
- Hock, T. F., and J. L. Franklin, 1999: The NCAR GPS dropwind-sonde. *Bull. Amer. Meteor. Soc.*, **80**, 407–420.
- James, P. K., and K. A. Browning, 1979: Mesoscale structure of line convection at surface cold fronts. *Quart. J. Roy. Meteor. Soc.*, **105**, 371–382.
- James, R. P., J. M. Fritsch, and P. M. Markowski, 2005: Environmental distinctions between cellular and slabular convective lines. *Mon. Wea. Rev.*, **133**, 2669–2691.
- Kessinger, C. J., P. S. Ray, and C. E. Hane, 1987: The Oklahoma squall line of 19 May 1977. Part I: A multiple Doppler analysis of convective and stratiform structure. *J. Atmos. Sci.*, **44**, 2840–2864.
- Keyser, D., M. J. Reeder, and R. J. Reed, 1988: A generalization of Petterssen's frontogenesis function and its relation to the forcing of vertical motion. *Mon. Wea. Rev.*, **116**, 762–781.
- Klemp, J. B., and R. B. Wilhelmson, 1978: The simulation of three-dimensional convective storm dynamics. *J. Atmos. Sci.*, **35**, 1070–1096.
- Koch, S. E., M. DesJardins, and P. J. Kocin, 1983: An interactive Barnes objective map analysis scheme for use with satellite and conventional data. *J. Climate Appl. Meteor.*, **22**, 1487–1503.
- Lee, B. D., and R. B. Wilhelmson, 1997: The numerical simulation of non-supercell tornadogenesis. Part I: Initiation and evolution of pretornadic mesocyclone circulations along a dry outflow boundary. *J. Atmos. Sci.*, **54**, 32–60.

- Lugt, H. J., 1979: The dilemma of defining a vortex. *Recent Developments in Theoretical and Experimental Fluid Mechanics*, U. Muller, K. G. Roesner, and B. Schmidt, Eds., Springer Verlag, 309–321.
- Markowski, P. M., and C. Hannon, 2006: Multiple-Doppler radar observations of the evolution of vorticity extrema in a convective boundary layer. *Mon. Wea. Rev.*, **134**, 345–373.
- , —, and E. Rasmussen 2006: Observations of convective initiation “failure” from the 12 June 2002 IHOP deployment. *Mon. Wea. Rev.*, **134**, 375–405.
- Marquis, J. N., 2005: Kinematic observations of misocyclones along boundaries during IHOP. M.S. thesis, Department of Meteorology, Pennsylvania State University, University Park, PA, 94 pp.
- , Y. P. Richardson, and J. Wurman, 2004: Observations of misocyclones along boundaries during IHOP. Preprints, 22d Conf. on Severe Local Storms, Hyannis, MA, Amer. Meteor. Soc., CD-ROM, 16A.5.
- Martin, H. G., 1973: Some observations of microstructure of dry cold fronts. *J. Appl. Meteor.*, **12**, 658–663.
- Matejka, T., 2002: Estimating the most steady frame of reference from Doppler radar data. *J. Atmos. Oceanic Technol.*, **19**, 1035–1048.
- Miles, J. W., and L. N. Howard, 1964: Note on heterogeneous shear flow. *J. Fluid Mech.*, **20**, 331–336.
- Mohr, C. G., L. J. Miller, R. L. Vaughn, and H. W. Frank, 1986: The merger of mesoscale datasets into a common Cartesian format for efficient and systematic analyses. *J. Atmos. Oceanic Technol.*, **3**, 143–161.
- Moore, G. W. K., 1985: The organization of convection in narrow cold-frontal rainbands. *J. Atmos. Sci.*, **42**, 1777–1791.
- Palmen, E., and C. W. Newton, 1969: *Atmospheric Circulation Systems: Their Structure and Physical Interpretation*. International Geophysical Series, Vol. 13, Academic Press, 603 pp.
- Parsons, D. B., and P. V. Hobbs, 1983: The mesoscale and microscale structure and organization of clouds and precipitation in midlatitude cyclones. Part XI: Comparisons between observational and theoretical aspects of rainbands. *J. Atmos. Sci.*, **40**, 2377–2397.
- Pauley, P. M., and X. Wu, 1990: The theoretical, discrete, and actual response of the Barnes objective analysis scheme for one- and two-dimensional fields. *Mon. Wea. Rev.*, **118**, 1145–1163.
- Rotunno, R., J. B. Klemp, and M. L. Weisman, 1988: A theory for strong, long-lived squall lines. *J. Atmos. Sci.*, **45**, 463–485.
- Roux, F., V. Marecal, and D. Hauser, 1993: The 12/13 January 1988 narrow cold-frontal rainband observed during MFD/FRONTS 87. Part I: Kinematics and thermodynamics. *J. Atmos. Sci.*, **50**, 951–974.
- Sanders, F., and C. A. Doswell III, 1995: A case for detailed surface analysis. *Bull. Amer. Meteor. Soc.*, **76**, 505–521.
- Shapiro, M. A., 1984: Meteorological tower measurements of a surface cold front. *Mon. Wea. Rev.*, **112**, 1634–1639.
- Simpson, J. E., 1969: A comparison between laboratory and atmospheric density currents. *Quart. J. Roy. Meteor. Soc.*, **95**, 758–765.
- Stonitsch, J., and P. Markowski, 2004: Evolution of boundary layer wind and moisture fields along a front during IHOP. Preprints, 22d Conf. on Severe Local Storms, Hyannis, MA, Amer. Meteor. Soc., CD-ROM, 16A.7.
- Straka, J. M., E. N. Rasmussen, and S. E. Fredrickson, 1996: A mobile mesonet for finescale meteorological observations. *J. Atmos. Oceanic Technol.*, **13**, 921–936.
- Trapp, R. J., and C. A. Doswell, 2000: Radar data objective analysis. *J. Atmos. Oceanic Technol.*, **17**, 105–120.
- Wakimoto, R. M., and B. L. Bosart, 2000: Airborne radar observations of a cold front during FASTEX. *Mon. Wea. Rev.*, **128**, 2447–2470.
- , and —, 2001: Airborne radar observations of a warm front during FASTEX. *Mon. Wea. Rev.*, **129**, 254–274.
- Weckwerth, T. M., and Coauthors, 2004: An overview of the International H₂O Project (IHOP) and some preliminary highlights. *Bull. Amer. Meteor. Soc.*, **85**, 253–277.
- Weisman, M. L., 1992: The role of convectively generated rear-inflow jets in the evolution of long-lived mesoconvective systems. *J. Atmos. Sci.*, **49**, 1826–1847.
- , and R. J. Trapp, 2003: Low-level mesovortices within squall lines and bow echoes. Part I: Overview and dependence on environmental shear. *Mon. Wea. Rev.*, **131**, 2779–2803.
- , J. B. Klemp, and R. Rotunno, 1988: Structure and evolution of numerically simulated squall lines. *J. Atmos. Sci.*, **45**, 1990–2013.
- Wurman, J., J. Straka, E. Rasmussen, M. Randall, and A. Zahrai, 1997: Design and deployment of a portable, pencil-beam, pulsed, 3-cm Doppler radar. *J. Atmos. Oceanic Technol.*, **14**, 1502–1512.
- Xue, M., and W. Martin, 2006: A high-resolution modeling study of the 24 May 2002 dryline case during IHOP. Part II: Horizontal convective rolls and convective initiation. *Mon. Wea. Rev.*, **134**, 172–191.
- Young, G. S., and R. H. Johnson, 1984: Meso- and microscale features of a Colorado cold front. *J. Climate Appl. Meteor.*, **23**, 1315–1325.
- , T. N. Sikora, and N. S. Winstead, 2005: Use of synthetic aperture radar in finescale surface analysis of synoptic-scale fronts at sea. *Wea. Forecasting*, **20**, 311–327.
- Yu, C.-K., and B. F. Smull, 2000: Airborne Doppler observations of a landfalling cold front upstream of steep coastal orography. *Mon. Wea. Rev.*, **128**, 1577–1603.